






Article

Selective Catalytic Reduction of NO_x by CO over Cu(Fe)/SBA-15 Catalysts: Effects of the Metal Loading on the Catalytic Activity

Monique S. Souza¹, Antonio J. Martins², Jackson Anderson S. Ribeiro¹, Adriana Campos³, Alcineia C. Oliveira^{2,*} , Raí F. Jucá⁴ , Gilberto D. Saraiva⁴ , Marco Antonio M. Torres⁵ , Enrique Rodríguez-Castellón⁶  and Rinaldo S. Araujo^{1,7}

¹ Instituto Federal de Educação-IFCE, Campus de Fortaleza, Av. 13 de Maio, Fortaleza 60040-531, Ceará, Brazil

² Departamento de Química Analítica e Físico-Química, Universidade Federal do Ceará, Campus do Pici, Bloco 940, Fortaleza 60455-760, Ceará, Brazil

³ CETENE, Cidade Universitária, Recife 50740-545, Pernambuco, Brazil

⁴ Faculdade de Educação, Ciências e Letras do Sertão Central, Universidade Estadual do Ceará, Quixadá 63902-098, Ceará, Brazil

⁵ Departamento de Física Teórica e Experimental, Universidade Federal do Rio Grande do Norte, Avenida Senador Salgado Filho, Natal 59078-970, Rio Grande do Norte, Brazil

⁶ Departamento de Química Inorgánica, Facultad de Ciencias, Universidad de Málaga, 29071 Málaga, Spain

⁷ Centro de Ciências e Tecnologia, Universidade Estadual do Ceará, Campus do Itaperi, Av. Doutor Silas Munguba, Fortaleza 60740-903, Ceará, Brazil

* Correspondence: alcineia@ufc.br

Abstract: Mesoporous Cu(Fe)/SBA-15 catalysts were prepared with distinct metal loadings of ca. 2–10 wt.%. A detailed set of characterizations using X-ray diffraction (XRD), electron paramagnetic resonance (EPR), transmission electron microscopy (TEM), scanning electron microscopy coupled to energy dispersive spectroscopy (SEM-EDS), Mössbauer spectroscopy, X-ray photoelectron spectroscopy (XPS) and Raman spectroscopy was performed to correlate the relationship among structure, electronic properties and catalytic performances. All solids were evaluated in the selective catalytic reduction of NO_x in the presence of CO (CO-SCR). The influence of the metal loadings on the overall activity indicated that introducing high amounts of Fe or Cu on the catalysts was beneficial to form either CuO or α -Fe₂O₃ clusters. Cu_x/SBA-15 series exhibited more efficient activity and poison-tolerant ability during CO-SCR reaction, in contrast to Fe_x/SBA-15. In spite of the Fe species introduced on SBA-15 having structural features similar to those of Cu ones, low interactions among Fe nanoparticles, silica and clusters impeded the high performances of Fe₁₀/SBA-15. XPS revealed the Fe species in a more oxidized state, indicating the stability of the solid after the catalytic tests, in agreement with EPR and Raman spectroscopy. Cu₈/SBA-15 worked better, being recyclable due to the interaction of the Cu²⁺ ions with SBA-15, avoiding the deactivation of the catalyst.

Keywords: SCR-CO; Cu; Fe; metal loadings; CuO clusters



Citation: Souza, M.S.; Martins, A.J.; Ribeiro, J.A.S.; Campos, A.; Oliveira, A.C.; Jucá, R.F.; Saraiva, G.D.; Torres, M.A.M.; Rodríguez-Castellón, E.; Araujo, R.S. Selective Catalytic Reduction of NO_x by CO over Cu(Fe)/SBA-15 Catalysts: Effects of the Metal Loading on the Catalytic Activity. *Catalysts* **2023**, *13*, 527. <https://doi.org/10.3390/catal13030527>

Academic Editor: Zhaoyang Fan

Received: 21 December 2022

Revised: 27 February 2023

Accepted: 28 February 2023

Published: 4 March 2023



Copyright: © 2023 by the authors. Licensee MDPI, Basel, Switzerland. This article is an open access article distributed under the terms and conditions of the Creative Commons Attribution (CC BY) license (<https://creativecommons.org/licenses/by/4.0/>).

1. Introduction

Selective catalytic reduction (SCR) is a promising technology involving reaction routes to control NO_x emissions from power plants, steel sintering boilers and waste incinerators [1–4]. This makes the SCR of hydrocarbon molecules and greenhouse gases, e.g., CO and CO₂, very attractive processes for an industrial application [3,5]. Through SCR reactions, NO_x is directly transformed into nitrogen and other molecules with high atom efficiency over a catalyst [5]. Such underlying processes meet the strict environmental and economic standards of NO_x mitigation and greenhouse gases abatement; thus, it is necessary to improve the SCR technology to target an efficient removal of the nitrogen oxides through catalytic reactions. Typically, strong reducing agents such as propane, ethanol, CO and H₂, among others are used to convert the nitrogen oxides and the aforementioned compounds into environmentally friendly chemical intermediates [3–9]. A persistent challenge

surrounding these methodologies, however, is achieving catalysts resistant against poisons to transform these processes into being cost-effective and industrially scalable.

The commercial V_2O_5 - MoO_3 / TiO_2 and V_2O_5 - WO_3 / TiO_2 catalysts applied in the conventional technology of selective catalytic reduction of NO_x through NH_3 have in common the fact that they show high activity when operating at high temperatures for long time interval processes operations [1,2,10]. In contrast, these Ti-based catalysts suffer from poor resistance to continual exposure to alkali metals, water, heavy metals, sulfur, ammonium salts and alkaline earth metals poisons [8,10]. Among other limitations of this approach, the low selectivities offered by the aforesaid catalysts play a critical role of undesired high by-product yields, besides the low catalyst lifetimes [1–5].

Alternatively, NO_x can also be reduced to N_2 by CO, i.e., CO-SCR over a variety of catalysts [6–8]. The CO is one of the most important components in diesel exhaust; thus, the selective catalytic reduction (SCR) with CO as the reducing agent is a proven effective denitration technology to remove NO_x in the flue gas from fixed and mobile sources [3,6,9]. The CO-SCR could expand the processing window for abatement of NO_x pollutant in conjunction with the CO greenhouse gas. Using poison-tolerant and stable catalysts in a broad range of temperatures could avoid the costs involved in the process' steps.

Various catalysts such as supported metal oxides, Cu-containing catalysts, and mesoporous aluminum silicates have been studied in the selective catalytic reduction of NO_x by CO [6,11–15]. Among these catalysts, Cu and Fe containing solids prepared through distinct methods show promise, even though a low resistance to SO_2 and water decreased their performance in the CO-SCR reaction [3,6]. In particular, copper and iron-based catalysts have shown promise for CO-SCR reaction owing to the excellent physical properties of the porous SBA-15 matrix with precisely controlled particles dispersed on it [6]. In addition, Cu^{2+} cations can act as Lewis acid sites, with these having a central role of enhancing the SCR activity owing to the activation of NO_x . Likewise, Fe^{3+} cations acting as Lewis acid sites have an affinity towards CO, and the iron species can simultaneously avoid the sulfur poisoning effects [6,11,12]. Moreover, the poisons could affect the formation of chemisorbed oxygen species on solid surface to a significantly greater extent than other catalysts [6,12]. An optimization of CO-SCR conditions has been also previously reported [6]. Unfortunately, the aforementioned Cu and Fe-based catalysts are still sensitive to deactivation through sulfur and water poisons. As these compounds compete for the metal active sites, NO_x conversions experience a drop at significant rates for long periods.

Therefore, the chemical structure of the porous SBA-15 must be altered to induce tailored properties by adding Fe and Cu active sites to enable high structural stability to the solids. As the catalyst design is a key issue in SCR, the achievement of highly tolerant solids to sulfur and water, and use of the solids on repeating cycles to reaction are a challenging task. To date, this issue has not been explored, although important contributions are found in the open literature [11–16].

In this work, the effects of the Cu and Fe loadings incorporated or dispersed on SBA-15 were investigated. The structural ordering of mesoporous catalysts influences the catalytic activity. As an alternative approach to address this issue, the roles played by Cu^{2+} (Fe^{3+}) species in exchange positions, oxide-like Cu(Fe) species inside the pores and Cu(Fe)-oxide clusters on the outer surface of the SBA-15 are intensively studied.

2. Results and Discussion

2.1. Physicochemical Characterizations

For SBA-15, Cu_x /SBA-15 and Fe_x /SBA-15 catalysts with metal contents lower than 2 wt.%, the diffraction peaks indicate the formation of an amorphous structure only (Figure S1, supplementary materials), which is an indication of the presence of the amorphous walls of SBA-15 [6]. Accordingly, poor-crystallized SBA-15 phase with a 2D hexagonal long-range mesopore ordered structure, e.g., $P6mn$ space group, appears through the (100), (110) and (200) planes [6,17,18]. Moreover, the interplanar distance d_{100} of the unmodified SBA-15 sample is 0.882 nm and the lattice parameter a_0 is 0.102 nm, in line with

the findings [6,9,13]. For Cu₂/SBA-15, the interplanar distance of ca. 0.898 nm and lattice parameter of ca. 0.103 nm both associated with the (100) plane suggest slightly higher values than that of pure SBA-15. This illustrates that some Cu²⁺ ions are present in the pores of the amorphous ordered silicate [18]. In contrast, XRD reflections of the samples with Cu loadings of less than 6.0 wt.% are broad and possess low intensity (Figure S1, supplementary materials). Additionally, the degree of crystallinity of Cu_x/SBA-15 samples increases when the Cu loading is close to 8.0 wt.% as in the case of Cu₈/SBA-15. Indeed, the appearance of the (110), (002), (111), (202), (020),(220) and (−311) planes of tenorite indicates the CuO arising as a separate crystalline species (Table 1). This is well consistent with the monoclinic CuO structure with the C2/c space group (JCPDS 03-0884) [3,13]. In addition, Table 1 illustrates that the Cu₈/SBA-15 has small particles measuring 9 nm on average while Cu₄/SBA-15 and Cu₆/SBA-15 have quite small particles in the range of 6–7 nm. Similar results demonstrate that part of the Cu species mainly exist highly dispersed inside the mesopores of SBA-15, while the other portion is on the external silica surface [19].

Table 1. Phases identified through XRD and composition of the catalysts in study.

Sample	Phase through XRD	Particle Size (nm)	^a Cu (wt.%)	^a Fe (wt.%)	^a Cu/Si Molar Ratio	^a Fe/Si Molar Ratio	^b Metal (wt.%)
SBA-15	Amorphous	-	-	-	-	-	-
Cu ₂ /SBA-15	Amorphous	-	1.6	-	0.015	-	-
Cu ₄ /SBA-15	CuO	6	2.4	-	0.023	-	1.2
Cu ₆ /SBA-15	CuO	7	4.8	-	0.047	-	5.1
Cu ₈ /SBA-15	CuO	9	8.9	-	0.090	-	7.1
Fe ₂ /SBA-15	Amorphous	-	-	2.7	-	0.014	2.2
Fe ₄ /SBA-15	Amorphous	-	-	3.6	-	0.021	-
Fe ₆ /SBA-15	α-Fe ₂ O ₃	4	-	6.1	-	0.040	4.7
Fe ₁₀ /SBA-15	α-Fe ₂ O ₃	4	-	10.1	-	0.076	11.6

^a Chemical analysis by atomic absorption spectroscopy. ^b Elemental analysis by EDS.

In the case of Fe_x/SBA-15 catalysts, its low crystallinity diffraction patterns are well-matched with that of SBA-15 for Fe loadings lower than 4.0 wt.% (Table 1). This could indicate the presence of Fe oxide-like species inside the pores of the support. When the loadings of Fe increased from 6 to 10%, the XRD reflections (Figure S1, supplementary materials) depict narrower and more intense diffraction peaks than that of pure SBA-15, indicating that some Fe species are formed into or on mesopores of SBA-15. Accordingly, relatively sharp diffraction peaks appearing at (012), (104), (110), (113), (024), (214), and (300) planes for Fe₆/SBA-15 and Fe₁₀/SBA-15 are associated with the well-crystallized hematite α-Fe₂O₃ phase [6]. In addition, the hematite phase belongs to a rhombohedral structure with R3C space group, in accordance with the JCPDS 39-1346 [14].

The crystal sizes of samples are not affected by increasing the Fe content more than 2.0 wt.%, i.e., below 4 nm, being characteristic of nanometric hematite phase, which is not detectable through XRD. Moreover, both the cell unit parameter the interplanar distance of ca. 0.896 nm and a₀ = 0.103 nm for Fe₂/SBA-15 indicate a possible substitution of Fe³⁺ ions onto SBA-15 exchange positions or dispersion of the Fe species on the mesoporous silicate, as found elsewhere [20]. Apparently, the aforesaid nanometric phase is physically mixed with the SBA-15 as a Fe silicate or yet forming Fe-oxide clusters on the outer surface of the SBA-15. The existence of these species is further confirmed via Mössbauer spectroscopy. The nominal compositions of Cu and Fe present in the samples are close to the theoretical calculations (Table 1). Additionally, Cu/Si and Fe/Si ratios increase as the metal component loadings increase owing to the structural changes occurred in the solids upon introducing the metals, in agreement with the findings [14]. Remarkably, Cu amounts obtained via EDS analyses have slightly lower values than those obtained through chemical analyses, which is suggestive of Cu species being mostly on the bulk of the solids. In contrast, the

augmentation of the Fe amount observed through EDS analyses is more pronounced on Fe₁₀/SBA-15, being an indicative of the Fe species being more finely dispersed on the SBA-15 surface. This also accounts for the Fe species most likely forming Fe clusters interacting with the support and partially blocking the pore system, especially in the case of the Fe₆/SBA-15 and Fe₁₀/SBA-15 samples, in accordance with the findings [21,22].

2.2. Raman and EPR Measurements

Raman spectra of selected samples are obtained to investigate the structural features of the solids upon addition of distinct Cu and Fe loadings (Figure 1a). As expected, vibration bands due to metal oxides incorporated into the solids are observed at a range of 200–1200 cm⁻¹ for all samples. For Cu_x/SBA-15 samples, the Raman spectra depict a very strong band near 287 (A_g) cm⁻¹ accompanied by a weak band at about 340 cm⁻¹ (B_g), which is obviously evidence of Cu₄/SBA-15. These bands reveal the presence of the tenorite CuO phase, as suggested by XRD. Moreover, CuO belongs to the C2/c space group (C₆^{2h}), with a monoclinic structure with two molecules per primitive cell [23–25]. This type of structure normally has three acoustic modes (A_u + 2B_u), six infrared active modes (3A_u + 3B_g) and three Raman active modes (A_g + 2B_g) [24]. Additionally, other bands found for Cu-containing samples are visible at 446, 493 and 623 (B_{2g}), corresponding to main modes of CuO, whereas those at 990 and 1111 cm⁻¹ can be ascribed to the Si–O vibrations in a structure unit with two and one non-bridging oxygen atoms per silicon, respectively [25]. Importantly, typical bands for bulk CuO do not shift upon varying the Cu loadings, although the band around 960 cm⁻¹ assigns for finely dispersed CuO species in strong interaction with surface silanol from SBA-15 support [24,25].

The main Raman bands for Fe_x/SBA-15 samples are poorly resolved, as illustrated in Figure 1a. Several weak bands appear in all samples at 222 (A_{1g}), 290 (E_g), 405 (E_g), 497 (A_{2g}), 610 (E_g) and 659 cm⁻¹ (LO E_u), which resembles more closely the bands of bulk α-Fe₂O₃. This is consistent with the XRD data. The hematite α-Fe₂O₃ phase belongs to the rhombohedral crystal structure with the R3C space group (D_{3d}⁶) and exhibits normal modes at the Brillouin zone center with seven active phonon modes (2A_{1g} + 5E_g), six IR-active vibrations (2A_{2u} + 4E_u) and five optically silent vibrations (2A_{1u} + 3A_{2g}) allowed in Raman and other bands at high frequencies regions [26–29]. The band at about 1073 cm⁻¹ belonging to the Si–O bands strongly suggests that Fe oxides nanoparticles lack a strong interaction with silica, independently of the iron loading.

In an attempt to further characterize the Cu and Fe valence states, EPR measurements are performed at room temperature. The EPR spectra of the Cu_x/SBA-15 samples (Figure 1b) exhibits a typical well-resolved and broad double-line shape with a g value of 2.18 in the magnetic field region of 2500–3500 Gauss. These features can be attributed to the presence of Cu(II) species, which is finely dispersed as copper oxide in a silicate matrix that has very similar results with low copper loadings [30,31]. This is especially true for Cu₄/SBA-15 with copper loadings lower than 4%. The EPR spectral shape reveals small-though resolvable changes at copper loadings superior to 4%, that is to say, the intensity decreases as a consequence of the hyperfine lineshape broadening. It could be indicative of the aggregation of the copper species in either small oligomeric CuO_x or magnetically isolated CuO clusters from the SBA-15 matrix that may still contribute to the EPR signal, as found elsewhere [30]. Moreover, the CuO clusters formation from a silica matrix in samples with high Cu loadings is evidenced in the Raman and XRD results. Noteworthy, Cu₈/SBA-15 depicts very weak EPR signal at the low-magnetic field region of 1000–2000 Gauss corresponding to the isolated Cu(II) ions, whereas the signal at g = 2.18 shifts to higher magnetic field regions, in comparison to the other samples. Such specific effect changes observed in the EPR spectrum of Cu₈/SBA-15 are probably due to the extremely small amount of the Cu²⁺ species included in the SBA-15 matrix, in addition to the presence of the aforesaid clusters. The EPR signals with weak intensities arise in low-field region for Cu-based silica samples because of the parallel component attributed

to the hyperfine interactions of Cu^{2+} cations in axial symmetry and Cu^{2+} in octahedral coordination [30].

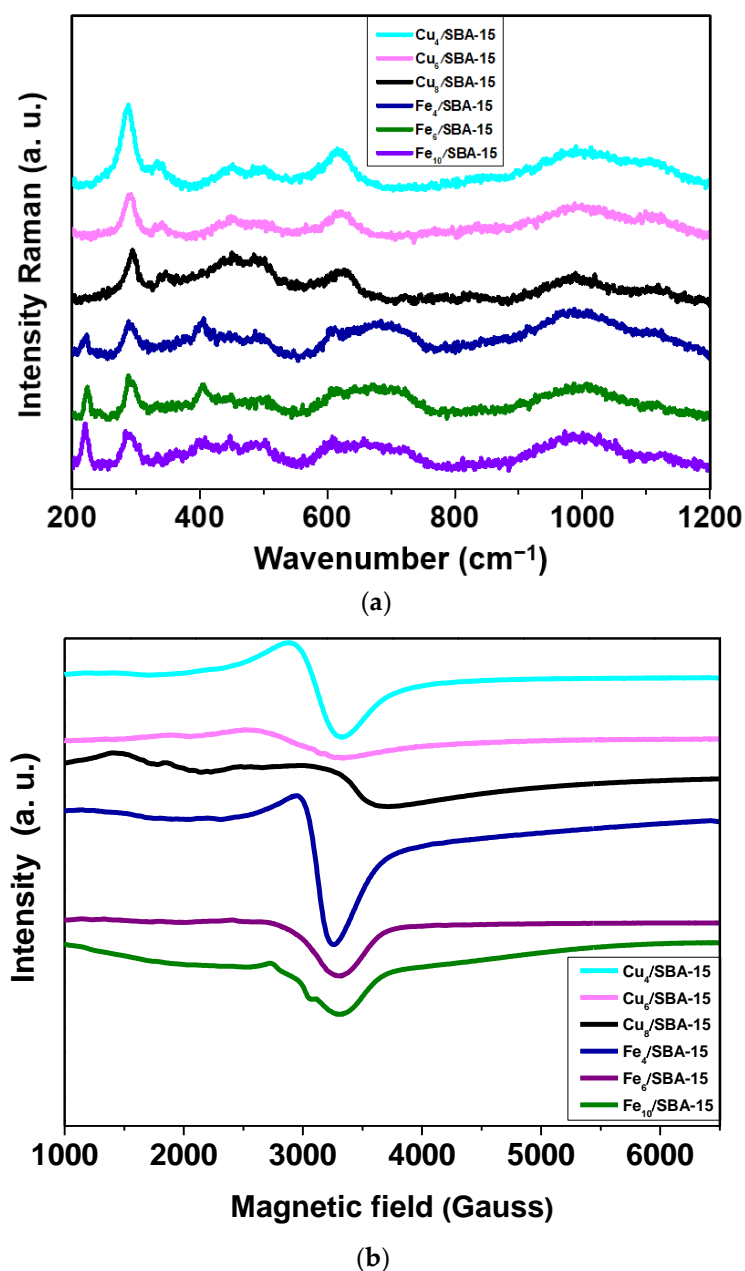


Figure 1. (a) Raman spectra of selected samples obtained in the range of 200–1200 cm^{-1} and (b) EPR spectra of selected samples taken at room temperature.

EPR spectra of $\text{Fe}_x/\text{SBA-15}$ catalysts are also shown in Figure 1b. A broad resonance linewidth is detected in all Fe-containing samples. It is worth mentioning that EPR spectrum of $\text{Fe}_4/\text{SBA-15}$ exhibits a more symmetric and intense resonance signal at around 3000 G with $g = 2.20$ and another weak signal at about 4.1. The first signal corresponds to the aggregated Fe^{3+} species in the form of small clusters of Fe^{3+} ions, while the signal of $g = 4.1$ is assigned to the formation of the isolated Fe^{3+} species located in axially distorted sites [32,33]. According to Raman and XRD measurements, Fe species are preferably found in a well-dispersed state in the SBA-15 matrix for samples with low Fe loadings. Meanwhile, the intensity of EPR signals continuously decreases by increasing the Fe amounts, which is accompanied by a lineshape broadening of the spectra. This can be understood considering

the intensity decrease observed for these signals owing to the formation of Fe silicate clusters, although there are still some Fe^{3+} isolated species. Moreover, these differences of the spectral features arise most likely with 4–10% Fe loadings, suggesting a covering of the solid surface by Fe clusters for $\text{Fe}_6/\text{SBA-15}$ and $\text{Fe}_{10}/\text{SBA-15}$ samples.

2.3. Morphology and Structure

SEM-EDS analyses are obtained to collect information about the morphology and elemental compositions of the solids. Representative SEM micrographs of $\text{Cu}_x/\text{SBA-15}$ (Figure 2A₁) and $\text{Fe}_x/\text{SBA-15}$ (Figure 2A₂) reveal a morphology constituted by interconnected and agglomerated nanofibers, independently of the type of metal dispersed on SBA-15. As previously reported [34,35], SBA-15 has typical rod-like particles and/or irregularly spherical morphology, in line with the obtained results. The Si and O are found in all samples, as shown by the EDS spectra (Figure 2B₁,B₂). Additionally, surface Cu and Fe amounts of 7.1 and 11.6 wt.% appear in $\text{Cu}_8/\text{SBA-15}$ and $\text{Fe}_{10}/\text{SBA-15}$, respectively. Moreover, elemental carbon arises from the support used to disperse the samples. It is evident that the Fe weight percentage is higher than that of Cu, with the former species having loadings quite close to the bulk, e.g., 10 wt.% of metal. This could be read as Fe being mostly on the SBA-15 surface, whereas Cu is located on the intraparticle voids or in the mesopores of SBA-15, with some of these Cu species existing in the form of agglomerated clusters. This is consistent with the Raman and EPR results and confirms that Fe is in a spatially homogeneous distribution on solid surface, in contrast with the Cu species.

TEM micrograph of $\text{Cu}_8/\text{SBA-15}$ illustrates some crystalline domains with the overall morphology of SBA-15 preserved (Figure 2C₁). Additionally, the interplanar spacing of 0.19 nm is assigned to the (111) plane of CuO particles, with sizes varying from 2–29 nm, being smaller compared to those of the $\text{Fe}_{10}/\text{SBA-15}$ sample. In addition, an interplanar spacing of 0.25 nm corresponding to the (104) plane of $\alpha\text{-Fe}_2\text{O}_3$ is observable in the TEM micrograph of $\text{Fe}_{10}/\text{SBA-15}$ (Figure 2C₂). Additionally, Fe particles seem to be agglomerated with an average size of approximately 3–40 nm. Moreover, Cu nanoparticles evidently appear agglomerated in $\text{Cu}_8/\text{SBA-15}$ (Figure 2D₁).

Additionally, these nanoparticles mainly comprise Cu-oxide clusters on the outer surface of the SBA-15 with some of these nanoparticles strongly interacting with the silicate matrix. The Fe particles predominantly consist of agglomerates with an irregular shape, with silica surrounding these particles, as seen in Figure 2D₂. Furthermore, the inset figure indicates that the Fe nanoparticles are physically mixed with the SBA-15 and forming Fe-oxide clusters, as well.

These results agree with the Raman and XRD results, which suggest the presence of both well-dispersed Cu nanoparticles stabilized in the silicate matrix, besides copper particles in the form of clusters, whereas Fe species are in a silicate and Fe-oxide clusters are on the surface of SBA-15.

The low velocity ^{57}Fe Mössbauer spectra of selected samples are performed to investigate the coordination environment and valence state of iron (Figure 3). All spectra depict similar features with an asymmetric doublet representing Fe species in the paramagnetic or superparamagnetic (SPM) regime. When recording the Mössbauer spectrum of $\text{Fe}_{10}/\text{SBA-15}$ at a velocity of $12 \text{ mm}\cdot\text{s}^{-1}$, the same asymmetric doublet as the one measured at $4.30 \text{ mm}\cdot\text{s}^{-1}$ is obtained. Also, there is not signal of other component.

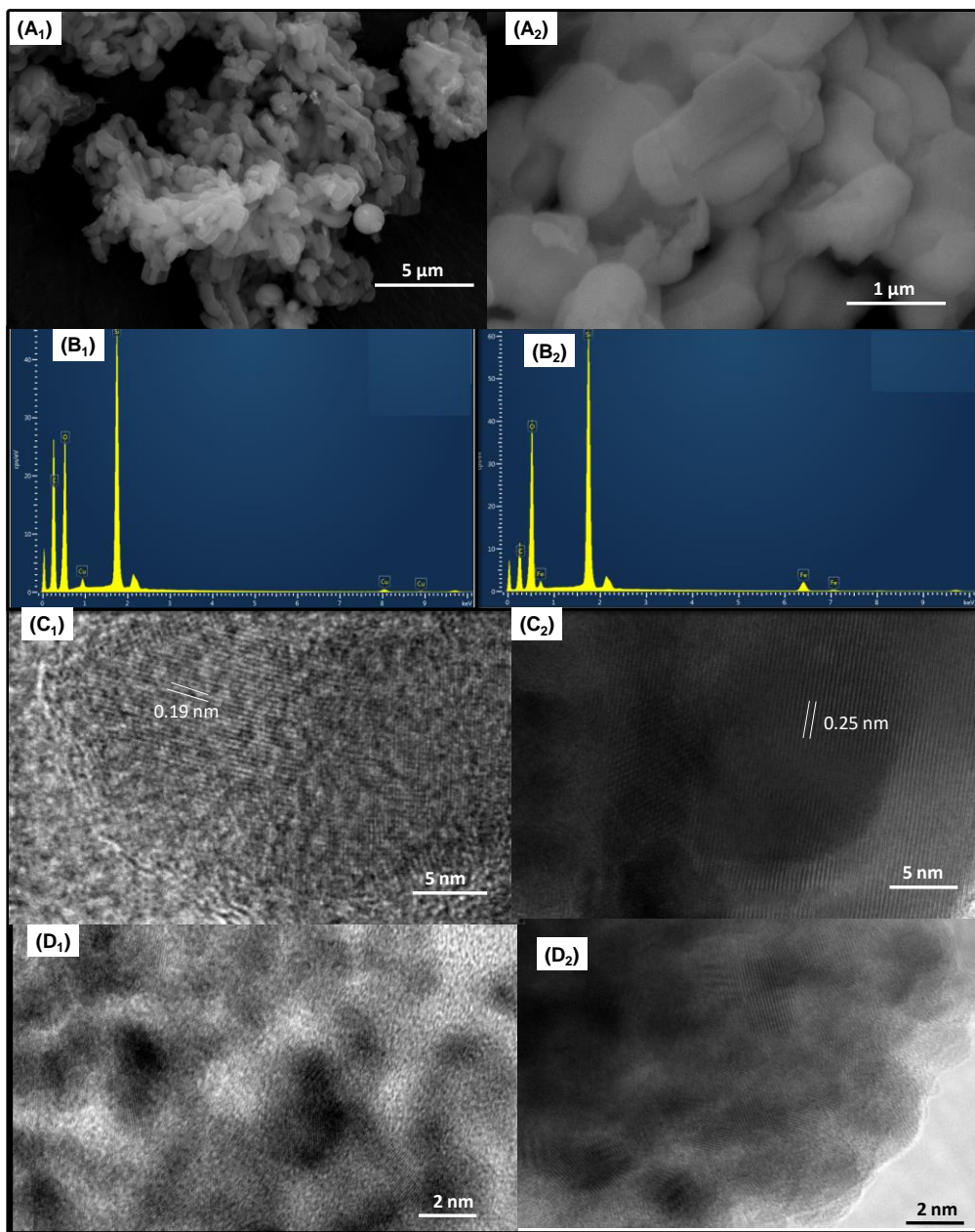


Figure 2. (A₁,A₂) SEM micrographs, (B₁,B₂) EDS spectra, (C₁,C₂) TEM and (D₁,D₂) HRTEM micrographs of the samples. The indices 1 and 2 below the letters indicate Cu₈/SBA-15 and Fe₁₀/SBA-15 samples, respectively.

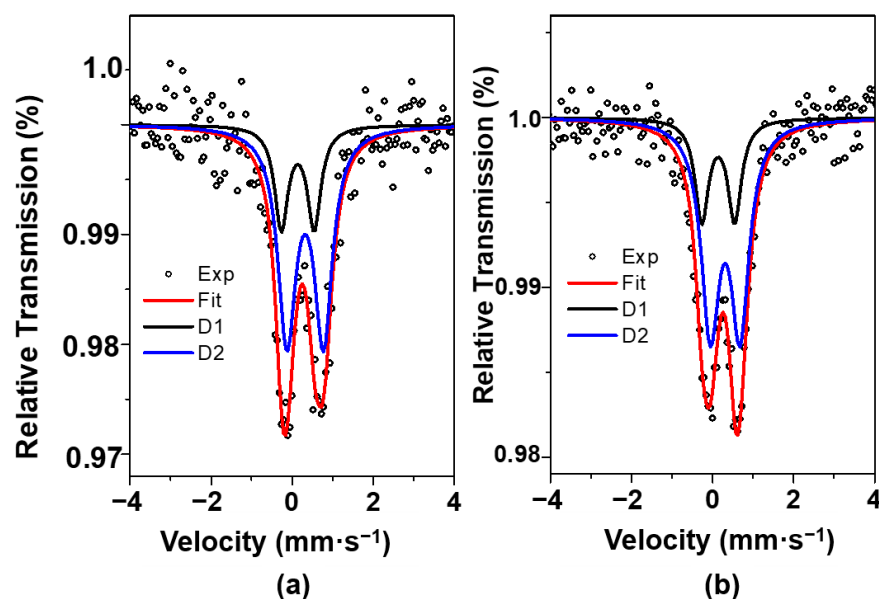


Figure 3. Mössbauer spectra of $\text{Fe}_x/\text{SBA-15}$ samples: (a) $\text{Fe}_6/\text{SBA-15}$ and (b) $\text{Fe}_{10}/\text{SBA-15}$.

The hyperfine parameters obtained from the Mössbauer spectra are summarized in Table 2.

Table 2. Hyperfine parameters obtained from Mössbauer spectra recorded at 27 °C.

Sample	Site	IS ($\text{mm}\cdot\text{s}^{-1}$)	QS ($\text{mm}\cdot\text{s}^{-1}$)	Width ($\text{mm}\cdot\text{s}^{-1}$)	Area (%)
$\text{Fe}_6/\text{SBA-15}$	D1	0.25	0.81	0.41	26
	D2	0.43	0.90	0.53	74
$\text{Fe}_{10}/\text{SBA-15}$	D1	0.24	0.80	0.40	27
	D2	0.42	0.75	0.54	73

Isomer shift (IS), quadrupole splitting (QS) and linewidth at half maximum (width) are in $\text{mm}\cdot\text{s}^{-1}$.

Both spectra are fitted to two doublets, namely D1 and D2, with isomer shifts and quadrupole splittings values similar to the ones presented for Fe^{3+} species [36]. In line with these results, Mössbauer spectra of Fe-based oxides have a doublet with the isomer shift of $0.30 \text{ mm}\cdot\text{s}^{-1}$ and quadrupole splitting of $0.76 \text{ mm}\cdot\text{s}^{-1}$, which may be related to superparamagnetic (SPM) Fe^{3+} species [37].

Moreover, D2 component features are probably assigned to the Fe species located in octahedral site in the hematite structure [38]. This suggests that these Fe^{3+} ions are present in the $\alpha\text{-Fe}_2\text{O}_3$ form, which possesses a small particle size and a very weak relationship with the support [39], in good agreement with the XRD and Raman results for samples with high Fe loadings.

It is well-known that hematite has a Néel magnetic transition at 682 °C with a paramagnetic regime above the aforesaid temperature. Below 682 °C, the Fe magnetic moments organize in two sublattices, forming an angle slightly smaller than 180°. Additionally, these moments have large antiparallel components, which lie on the a-b basal plane.

The small tilt angle of the moments with the basal plane favors the development of a small ferromagnetic moments perpendicular to the a-b plane. The weak ferromagnetic regime remains until $-13 \text{ }^\circ\text{C}$, which is known as the Morin transition, and below this temperature, the moments rotate to the c axis and an antiferromagnetic regime is established [40]. Because $\alpha\text{-Fe}_2\text{O}_3$ nanoparticles have a ferromagnetic signal and their particle sizes are smaller than the critical size for the formation of single magnetic domains, hematite may be in the SPM regime at room temperature owing to the thermally activated fast relaxation of Fe magnetic moments. Moreover, the relaxation time of these moments is smaller than the Mössbauer spectroscopy measuring time, which is typically $\sim 10^{-8} \text{ s}$.

In addition, the presence of the D1 doublet is attributed to the existence of Fe³⁺ ions in a silicate environment. This component has indeed a spectral contribution of 26%, indicating that a smaller amount of the total iron is forming the Fe-silicate phase in the Fe_x/SBA-15. Furthermore, hyperfine parameters of component D1 with the isomer shift of 0.25 mm·s⁻¹ and 0.80 mm·s⁻¹ are associated with poor crystallized iron silicates [40,41]. Besides, Fe nanoparticles in Fe-mesoporous silicate catalysts depict very broad doublet for Mössbauer spectra, which is typical of small sized hematite nanoparticles [41].

To further determine the surface chemical composition of selected fresh and spent solids, e.g., Cu₈/SBA-15 and Fe₁₀/SBA-15, XPS analyses are conducted. Table 3 shows the binding energy values (in eV) of the C 1s, O 1s, Si 2p and Cu 2p_{3/2} and Fe 2p signals.

Table 3. Si 2p, C 1s, O 1s, Cu 2p_{3/2}, Fe 2p_{3/2} binding energy values (in eV) of the selected samples.

Sample	Si 2p	C 1s	O 1s	Cu 2p _{3/2}	Fe 2p _{3/2}	Isat/Imp*
SBA-15	103.7	284.8 (78) 286.4 (18) 289.0 (4)	533.0			
Cu ₈ /SBA-15 fresh	103.5	284.8 (75) 286.3 (19) 288.8 (6)	530.1 (2) 532.8 (98)	933.5 936.2		0.42
Cu ₈ /SBA-15 used	103.4	284.8 (75) 286.5 (18) 288.9 (7)	530.3 (2) 532.8 (98)	933.8 936.1		0.45
Fe ₁₀ /SBA-15 fresh	103.5	284.8 (77) 286.5 (18) 288.6 (5)	530.4 (4) 532.9 (96)		710.7	
Fe ₁₀ /SBA-15 used	103.5	284.8 (78) 286.5 (17) 288.7 (5)	530.3 (4) 532.9 (96)		711.0	

Values in parentheses are % of each contribution in deconvoluted spectra. Isat/Imp* means Area of Cu 2p_{3/2} satellites/Area of Cu 2p_{3/2} main peak.

The Si 2p core level for SBA-15 support has a maxima at about 103.5 eV, which is typical of Si(IV) of silica [42,43]. There is an observable shift of 0.3 eV in the binding energy of silicon for the metal oxide/SBA-15 materials, indicating the occurrence of the silicon atoms mostly perturbed by a foreign ion such as Fe(III). At least, part of the active Fe phases is in the form of small clusters, while even individual Fe cations in the form of oxides are found on the surface of both fresh and spent catalysts. Thus, it is undecided whether small clusters of iron and silica in the form of silicates or individual cations are bonded to silicon, according to the XPS results.

All the C 1s core level spectra can be decomposed in three contributions with the main component having binding energy at 284.8 eV, which is related to the adventitious carbon (-C-C and -C=C- groups), as described earlier [8,43,44]. The second contribution at about 286.5 eV is due to C-OH or C-O-C bonds, whereas the third contribution appearing at high binding energy of ca. 288.6–289.0 eV is associated with carboxylate or carboxylic groups [44]. These species most probably arise in the spent samples from the chemisorbed byproducts formed on solid surface after the reaction.

The O 1s signal appears at 532.8–533.0 eV, typical of oxygen of silica. In the case of the Cu and Fe-silicas, an additional very weak contribution at 530.1–530.4 eV is observable. This is assigned to lattice oxygen of copper or iron oxides, as shown in the iron and copper silicates [24,28].

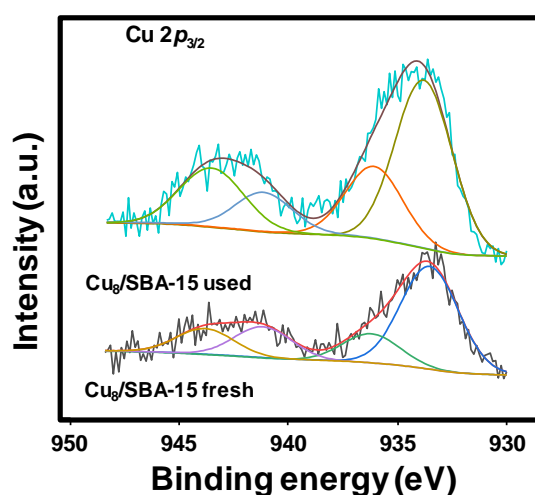
Table 4 depicts the surface chemical composition (in wt.%) of selected solids. As expected, both SBA-15 and metal oxide/SBA-15 materials have a very low content of adventitious carbon due to the hydrophobic nature of the mesoporous silica with a very low concentration of surface silanol group (Table 4).

Table 4. Surface chemical composition (in wt.%) of the selected samples determined by XPS.

Sample	C	O	Si	Cu	Fe	M/Si *
SBA-15	3.62	53.10	38.90			
Cu ₈ /SBA-15 fresh	4.90	51.33	37.36	4.38		0.050
Cu ₈ /SBA-15 used	4.76	53.08	37.81	6.41		0.076
Fe ₁₀ /SBA-15 fresh	4.93	53.03	37.38		4.35	0.058
Fe ₁₀ /SBA-15 used	5.82	53.51	40.67		4.65	0.062

* Molar ratio.

The Cu $2p_{3/2}$ core level spectra of the fresh and used samples are shown in Figure 4. The Cu $2p_{3/2}$ spectra can be decomposed into four contributions with the main peaks at 933.5 and 936.2 eV for Cu₈/SBA-15 fresh sample. The former contribution at 933.5 eV is assigned small clusters of copper interacting with the support, or even reduced copper, and the high binding energy contribution (936.2 eV) is ascribed to the presence of CuO particles [24,43].

**Figure 4.** Cu $2p_{3/2}$ core level spectra for Cu₈/SBA-15 fresh and used samples.

The fresh catalyst shows an I_{sat}/I_{mp} value of 0.42 (Table 3), which is lower than that observed for CuO (0.45). This indicates the presence of partially reduced copper species. In the case of the Cu₈/SBA-15 used sample, the Cu $2p_{3/2}$ spectra are decomposed into four contributions, the main peaks being at 933.8 and 936.1 eV. The Cu₈/SBA-15 fresh sample has similar binding energies, but the relative intensity of the contribution at 936.1 eV decreases and the I_{sat}/I_{mp} value is ca. 0.45, being slightly higher than the spent solid.

The most interesting fact is an increment of the Cu/Si ratio after the catalytic test (0.050 for the fresh catalyst, while that of used solid is 0.076) as shown in Table 4. This is indicative of an enrichment of Cu on the surface, after the catalytic evaluations. Indeed, both values are lower than that determined through atomic absorption spectrometry, 0.090, as shown in Table 1. The surface concentration of Cu in the used samples is 4.38 and 6.41 wt.% for the Cu₈/SBA-15 and Cu₁₀/SBA-15 samples, respectively (Table 4). Both values are lower than those found for the fresh samples, e.g., 8–10 wt.%. This means that a high proportion of Cu is inside the channels of the mesoporous silica, being inaccessible for XPS analysis.

The Fe $2p$ core level spectra for fresh and used Fe₁₀/SBA-15 samples (Figure 5) have very similar contributions, with the Fe $2p_{3/2}$ maxima being at 710.7 and 711.0 eV. This is in accordance with the reported binding energy values of the α -Fe₂O₃ phase [45], which is in line with the XRD, Raman and Mössbauer results that identified the hematite phase.

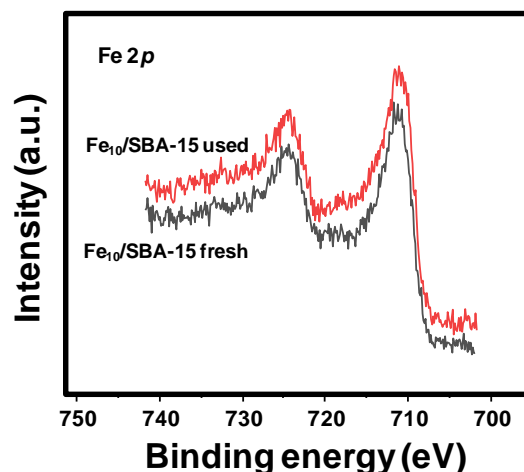


Figure 5. Fe 2p core level spectra for Fe₁₀/SBA-15 fresh and used.

Additionally, surface Fe/Si molar ratios determined through XPS are 0.058 and 0.062 (Table 4), again lower than that determined via atomic adsorption spectrometry (0.076). It could be suggestive of the surface of the solids being less rich in the active phase than the bulk.

Based on the XPS results, Fe appears to be more oxidized in Fe₁₀/SBA-15 used, being indicative of the stability of the solid after the catalytic tests, as indicated through EPR and Raman spectroscopy.

2.4. Catalytic Results

2.4.1. Effect of the Temperature, and NO_x to CO Molar Ratios

The CO-SCR reaction is conducted in the presence of the Cu_x/SBA-15 and Fe_x/SBA-15 series of mesoporous catalysts. Figure 6 clearly reveals that all catalysts show very low NO_x conversions at temperatures inferior to 250 °C.

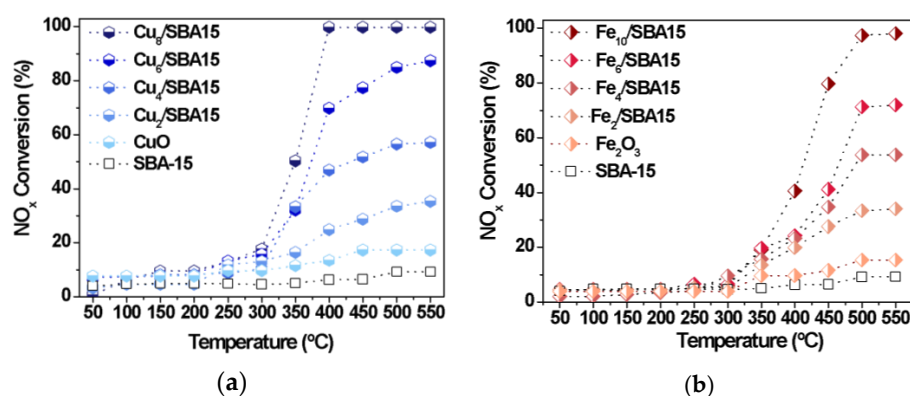


Figure 6. NO_x conversions as a function of the temperature. (a) Cu_x/SBA-15 and (b) Fe_x/SBA-15 series of solids.

As expected, SBA-15 is inactive in the reaction, whereas bulk CuO and α-Fe₂O₃ exhibit a low catalytic performance in all ranges of temperature studied.

The poor activity of the supported catalysts at low temperatures is mainly due to the NO_x species attached to the surface of the catalyst from various nitrate and nitrite species, which are not decomposed into N₂ at temperatures below 250 °C, as found elsewhere [21,45]. Additionally, the NO_x adsorption inhibits CO chemisorption to a certain extent at temperatures below 250 °C [45].

Nearly 300 °C, all NO_x species are further converted and CO molecules simultaneously react with the former species attached on the catalyst surface to form N₂. This is due to

the fact that the α -Fe₂O₃ and CuO phases present in the catalysts can absorb more NO_x species on the surface to form the isocyanate intermediate and its further conversion to nitrogen [3,45]. The presence of the aforesaid metal oxides is confirmed via Raman, XRD and Mössbauer spectroscopy.

It is worthy nothing that conversions of NO_x significantly increase at temperatures above 250 °C, with samples possessing Cu or Fe loadings close to 10 wt.% reaching full NO_x conversion within 500 and 550 °C (Figure 6). Thus, the metal loadings have a significant influence on enhancing the catalytic performance of the Cu_x/SBA-15 and Fe_x/SBA-15 catalysts. For instance, suitable loadings of metals as those inferior to 4.0 wt.% are able to promote the catalytic activity with NO_x conversions as high as 10% at 350 °C. On the other hand, conversion of NO_x reaches more than 20% at the same temperature promoted by the paramagnetic species present on the catalysts, especially the Fe-silicates clusters and Fe isolated species or the Cu species dispersed on SBA-15 surface, as suggested by the physicochemical characterizations of the solids. Additionally, Cu_x/SBA-15 series of solids (Figure 6a) are found to be more active Fe_x/SBA-15 than ones (Figure 6b) when the CO-SCR reaction is carried out at 350 °C for metal loadings of ca. 4–6%. The performance of the Fe_x/SBA-15 can be ascribed to the CO coordination to Fe³⁺ species at metal loadings superior to 6%. As a consequence, the reaction with N₂O leads to the N₂ and CO₂ without a change of the Fe valence state [20]. For all of the studied catalysts, the bulk α -Fe₂O₃ and CuO are less active than all the supported solids achieving NO_x conversions below 15% in the whole temperature regions. The difference in activities comparing bulk solids and the supported catalysts might be attributed to the presence of iron and copper species well-dispersed on solid surface or inside the pores of the latter or yet, forming metal clusters, which might be resistant against sintering effects due to their strong interaction with the support.

Based on the mechanistic considerations for CO-SCR and CO oxidation reactions [46–50], the Cu species are responsible for the redox property towards NO_x conversion with the contribution of the surface active oxygen species. The CO may be adsorbed on the Cu⁺ species while the latter is then stabilized at the interface of Cu reacting with lattice oxygen to form the CO₂. The subsequent rearrangement of the oxygen vacancies and Cu⁺ ions provide their transformation into the corresponding original species through re-oxidation, as observed in the literature for Cu-based catalysts in oxidation reactions [48,50]. In the case of Fe-based catalysts, NO_x species are adsorbed on the vacancy of the solids, leading to the dissociation of the former into [N] and [O] radicals, as found elsewhere [46,47]. In this route, the capture of the reactive oxygen species present on the catalysts by the CO molecules is highly favored. Additionally, N–O bonds are weakened and this may facilitate the dissociation of the NO_x species. Simultaneously, CO molecules react with [O] to form CO₂, while other [N] interacts with NO to form N₂O or with another [N], resulting in N₂, based on Langmuir–Hinshelwood mechanism at low temperatures and the Eley–Rideal mechanism at high temperatures [47].

Further studies on the effects of the NO_x to CO molar ratios during the CO-SCR reaction are carried out in the absence of oxygen. In addition, the Fe₁₀/SBA-15 and Cu₈/SBA-15 catalysts are chosen amongst all synthesized solids due to their superior performances. At temperatures lower than 250 °C, NO_x conversions achieve less than 15% (Figure 7), as a result of the low activation of the NO_x species and its subsequent decomposition into N₂.

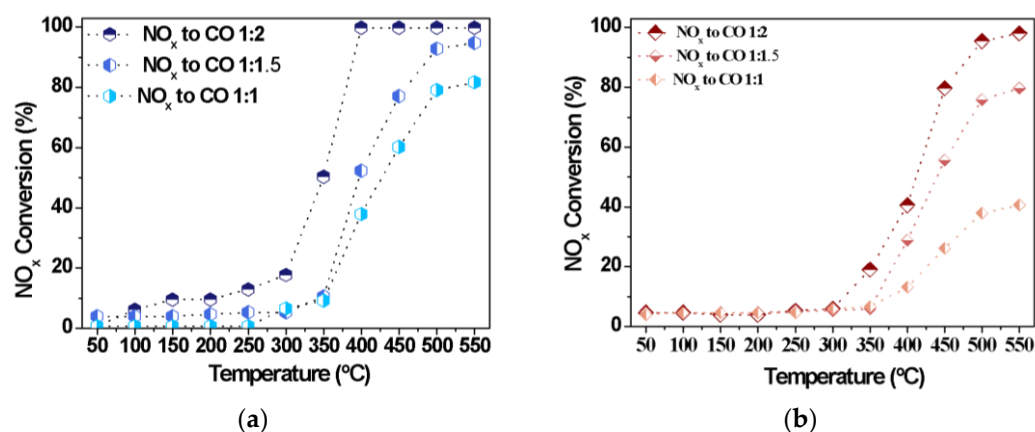


Figure 7. NO_x conversions as a function of the temperature for distinct NO_x to CO molar ratios over (a) Cu₈/SBA-15 and (b) Fe₁₀/SBA-15 samples.

A considerable increase in NO_x conversions is observed with increasing the reaction temperature over both catalysts, independently of the NO_x to CO molar ratios evaluated. The performances of catalysts are also comparable with distinct NO_x to CO molar ratios at a fixed temperature of 350 °C. Upon increasing the CO amounts, the activity of Cu₈/SBA-15 (Figure 7a) surpasses 50%, remaining higher than that corresponding to Fe₁₀/SBA-15 for a NO:CO of 0.5. This may be attributed to the contribution of the coverage of CuO active species on the external surface of the support or near the pores facilitating the CO oxidation and the consequent interaction of CO with NO_x [48–50]. However, the low catalytic performance of Fe₁₀/SBA-15 (Figure 7b) is directly associated with the Fe loadings, since the deposition of Fe species on the support may result in larger bulky Fe clusters with limited activities, even if there are more adjacent surface Brønsted and Lewis acid sites coming from the Fe species [20]. The catalysts reach their highest activities using the NO_x-to-CO molar ratios of 0.5 at temperatures above 350 °C. This is consistent with the fact that lower temperatures would result in the insufficient NO_x activation and fewer active CO molecules. Another significant finding in this work is that the activity in CO-SCR reaction is related to the loadings of metals; in particular, Fe₁₀/SBA-15 and Cu₈/SBA-15 exhibit an appreciably elevated activity at high temperatures. On the other hand, the catalyst properties, for example, accessible porosity and the dispersion of the metals, also play an important role in the CO-SCR reaction. In general, increasing the NO:CO molar ratio leads to a great improvement of the catalytic performance.

The turnover frequency values at various temperatures for Cu₈/SBA-15 and Fe₁₀/SBA-15 catalysts are shown in Figure S2, supplementary material. The TOF reaches values below $1.5 \times 10^{-3} \text{ s}^{-1}$ at temperatures lower than 300 °C for both samples and upsurges at temperatures superior to 350 °C similar to the NO_x conversion behavior. In the case of Cu₈/SBA-15, which shows a much higher TOF in the range of $4.1\text{--}7.5 \times 10^{-3} \text{ s}^{-1}$ and offered high NO_x conversions, e.g., 50–100% in the 350–400 °C range, a decrease in the TOF value to $6.2 \times 10^{-3} \text{ s}^{-1}$ is at temperatures up 400 °C. This could be attributed to the favorable NO_x adsorption on exposed unpaired Cu sites to form the nitrites and nitrates already at low temperatures; thus, CO reacts with NO_x species to form N₂ and CO₂, as found elsewhere [47–50]. In contrast, the TOF value is ca. $4.5 \times 10^{-3} \text{ s}^{-1}$ for Fe₁₀/SBA-15 at temperatures superior to 400 °C and the parameter is kept constant in comparison to its Fe₁₀/SBA-15 counterpart. The CO oxidation occurrence at temperatures lower than 400 °C and/or the decomposition of the isocyanate intermediate formed over a well-defined temperature range only explains the Fe sites behavior, as demonstrated elsewhere [20,46].

The turnover frequencies for Cu₈/SBA-15 and Fe₁₀/SBA-15 at 400 °C are calculated to be as 7.5×10^{-3} and $2.3 \times 10^{-3} \text{ s}^{-1}$, respectively. It is apparent that a major exposition of surface redox Cu active sites for the reactants compared with that of Fe, which in turn determine the excellent catalytic performance of the former solid.

2.4.2. Effect of the Oxygen Concentrations

To evaluate the effect of oxygen on the NO_x performance of Fe₁₀/SBA-15 and Cu₈/SBA-15 in CO-SCR, a step-response experiment was performed at various temperatures with a fixed NO_x to CO molar ratio of 0.5 (Figure 8). Amounts from 0 to 1000 ppm are usually applied to evaluate the catalyst tolerance to oxidation [51–53].

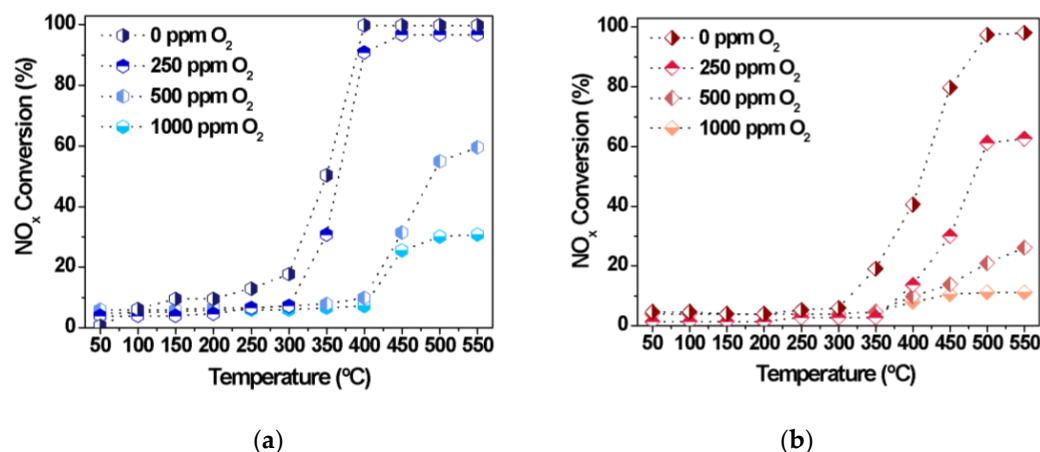


Figure 8. NO_x conversions as a function of the temperature in the presence of distinct amounts of oxygen over (a) Cu₈/SBA-15 and (b) Fe₁₀/SBA-15 samples.

Interestingly, the CO-SCR activities increase with rising reaction temperature, although the increased amount of oxygen deteriorates the catalytic performance of both solids. For instance, NO_x conversions gradually decrease from 100 to 20%, affording very low conversions if both catalysts are oxidized with high oxygen concentration above 1000 ppm at high temperatures (Figure 8a,b). The decrease in activity unambiguously suggests that NO_x would certainly encounter greater resistance to react with the Fe and Cu active sites owing to the competition provided by oxygen for these sites. The affinity of CO for oxygen to form CO₂ could impede the diffusion and adsorption of NO_x molecules on the oxidized Fe and Cu surface and this may be an additional reason for the poor performance of the solids in the CO-SCR reaction.

Thus, the optimized conditions for the CO-SCR reaction are at 400–550 °C and NO_x to CO molar ratio of 0.5 with a catalytic performance highly dependent on the extent of oxidation using very low or null amounts of oxygen. Thus, oxygen is able to preferentially react with CO and inhibit NO_x reduction during the CO-SCR reaction.

2.4.3. Effect of H₂O and SO₂ Poisons

Figure 9 shows the influence of steam poison on the NO_x conversion with temperature at a fixed NO_x to CO molar ratio of 1 with 0 ppm of oxygen. Water vapor may act as a strong oxidant in catalytic reaction involving metal based-catalysts, and is used as a probe molecule in the reduction of NO_x by CO at low temperatures to evaluate the resistance of catalysts against water vapor poison deactivation [5,48,52]. It can be observed that the NO_x conversion values exhibit a trend toward increasing with temperature and the catalytic performances vary almost linearly in the 300–400 °C range and remain constant beyond 500 °C. At 400 °C, the NO_x conversion of Cu₈/SBA-15 (Figure 9a) stabilizes, reaching nearly full conversion with a NO_x to CO molar ratio of 0.5 and 0 ppm oxygen, whereas that of Fe₁₀/SBA-15 is achieved only at 500 °C with similar conditions. The effect of the water vapor on the activity is that an appreciable decline in NO_x conversion is observed, compared to the absence of the poison. It can also be noticeable that at low temperatures (50–300 °C), all NO_x conversions are lower, but such effects of the water vapor presence are detected in both catalysts. This is especially important above 350 °C for Cu₈/SBA-15 (Figure 8a) while this trend is more noticeable for Fe₁₀/SBA-15 at 350 °C (Figure 8b).

Moreover, steam adsorption can contribute to the competitiveness or limit the Cu and Fe active sites, causing their deactivation with Fe species being sensitive to strong water adsorption; therefore, the NO_x conversion levels achieved with Fe₁₀/SBA-15 are quite low. As has been found elsewhere, the formation of cyanate/isocyanate intermediate species during the CO-SCR reaction is inhibited in the presence of steam by decreasing the catalytic performance [51].

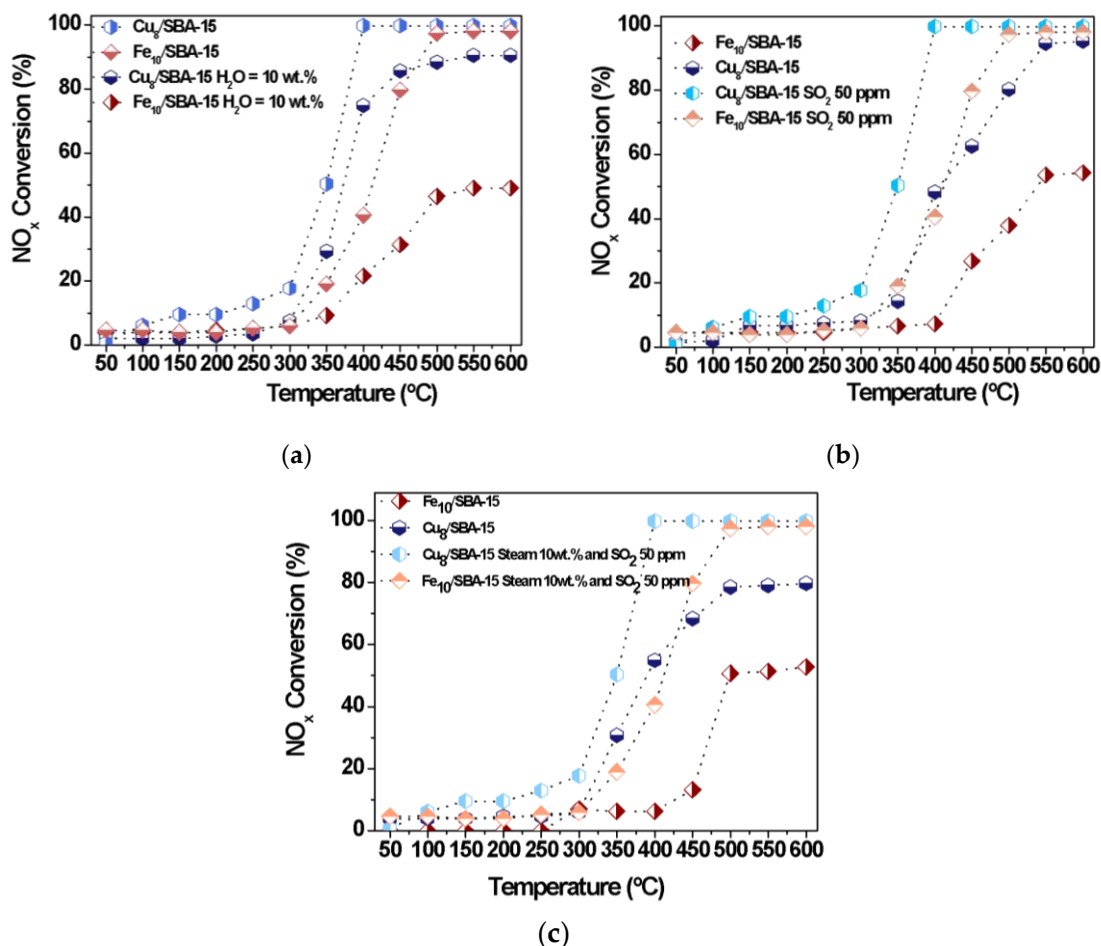


Figure 9. NO_x conversions as a function of the temperature in the presence of distinct poisons (a) Steam 10 wt.%, (b) SO₂ 50 ppm and (c) both steam 10 wt.% and SO₂ 50 ppm.

Most probably, CuO dispersed on SBA-15 or Cu clusters mainly facilitates weak interactions with CO and its oxidation in the presence of water vapor is not favored; thus, large amounts of residual CO may interact with NO_x, increasing the catalytic performance of the solid.

Moreover, the effects of SO₂ poison on the catalytic performance of Cu₈/SBA-15 and Fe₁₀/SBA-15 are carried out at various target temperatures (Figure 9b). The use of SO₂ as a poison significantly decreases the conversion of NO_x throughout the whole temperature range, in line with the widely reported detrimental SO₂ effects decreasing catalytic performances [49–51]. It seems reasonable that the inhibiting influence of SO₂ on the active sites results in little or no deactivation of the solids at temperatures below 350 °C since the NO_x conversions achieved with both catalysts are quite low. However, Figure 9b demonstrates that an imperative role of SO₂ in the poisoning of active sites is expected due to its strong adsorption on Fe and Cu [5,52–54]. Although the Fe species has the ability of being reversibly reduced and reoxidized during N₂O conversions [20], a fast decline in NO_x conversion is observed at temperatures above 350 °C for Fe sites in Fe₁₀/SBA-15. It is well-known that Fe species have a strong ability to interact with SO₂, forming inactive

ferrous sulfate or ferric sulfate, which blocks the active Fe^{3+} center [52–54]; consequently, this would reduce the capture of NO_x and CO by the Fe active sites. Notably, $\text{Cu}_8/\text{SBA-15}$ exhibits an enhanced SO_2 resistance ability with increasing temperature mainly due to the fact that the copper sulfate formed on Cu sites is less stable and decomposes in the range of 350–500 °C [53]. In other words, $\text{Cu}_8/\text{SBA-15}$ successfully combines the stability of Cu sites clusters on SBA-15 against SO_2 and steam with the high NO_x reduction by CO to form CO_2 and N_2 activity, achieving NO_x conversions to nearly 90% at 500 °C.

When both SO_2 and water vapor are used as poisons (Figure 9c), the catalytic performances of the solids follow a similar behavior to those of individual poisons and the NO_x conversions drop dramatically to values below 15% at temperatures inferior to 350 °C. As the temperature increases, the NO_x conversions of $\text{Fe}_{10}/\text{SBA-15}$ gradually rise but are still lower than those of $\text{Cu}_8/\text{SBA-15}$. This result clearly indicates that the sulfates and sulfuric acid formation on iron sites are the main factor for the deactivation of the former solid at relatively low temperatures of nearly 400 °C [3]. In contrast, a relatively higher catalytic activity is achieved at temperatures above 400 °C due to the fact that heating facilitates the breaking of the Fe-S bond, thereby providing better availability of the Fe active centers for NO_x and CO. In the case of $\text{Cu}_8/\text{SBA-15}$, NO_x conversions experience a decay at low temperature, but activity increases significantly in the whole temperature range. The highest NO_x conversion is 75% at 400 °C, which is thought to be due to the resistance of Cu sites to simultaneous SO_2 and water vapor poisons.

Figure 10 illustrates the catalytic performance of solids in the presence of both SO_2 and water vapor as a function of time on stream. The result reveals that the NO_x conversion achieved a plateau over the whole period of time and the solids had lower NO_x conversions compared to no poisons. Moreover, the NO_x conversion of 80% for $\text{Cu}_8/\text{SBA-15}$ is observed within 480 min, while that of $\text{Fe}_{10}/\text{SBA-15}$ declined to about 50%. Simultaneous H_2O and SO_2 poisons do not significantly affect the catalytic performance of solids, compared with the use of the individual poisons (Figure 9). This is mainly because an excess of water vapor leads to the limitation of the SO_2 poison on Fe and Cu sites owing to the direct reaction of H_2O with SO_2 causing a drop in the water vapor amounts that would further react through competitive adsorption with the CO, therefore, benefiting the catalytic performance of the solids within 480 min.

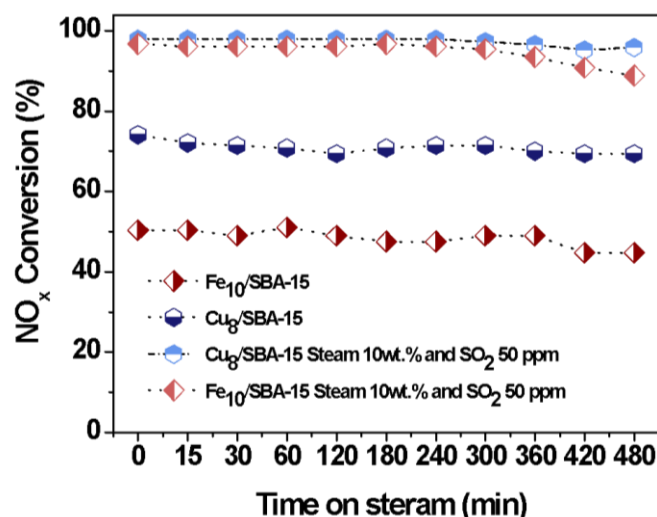


Figure 10. NO_x conversions as a function of the time on steam in the presence of distinct poisons: Steam 10 wt.%, SO_2 50 ppm and both steam 10 wt.% and SO_2 50 ppm.

On the other hand, the occurrence of $\text{Cu}^+/\text{Cu}^{2+}$ redox cycles in the presence of both poisons, as well as the adsorption capabilities for CO and NO_x , account for the difference in catalytic activity between $\text{Cu}_8/\text{SBA-15}$ and $\text{Fe}_{10}/\text{SBA-15}$.

Thus, the CO-SCR activity of $\text{Cu}_8/\text{SBA-15}$ is higher than that of $\text{Fe}_{10}/\text{SBA-15}$, indicating that there was some synergistic effect among the Cu nanoparticles dispersed on the SBA-15 matrix, the Cu silicate and Cu clusters, thus improving resistance against poisons.

Long term stability runs are carried out to illustrate the catalytic performance of solids under distinct conditions of temperature and time on stream (Figure 11). By running the CO-SCR reaction in the absence of poisons, NO_x conversions steadily increase at temperatures below 250 °C and speeds in the 300–350 °C range.

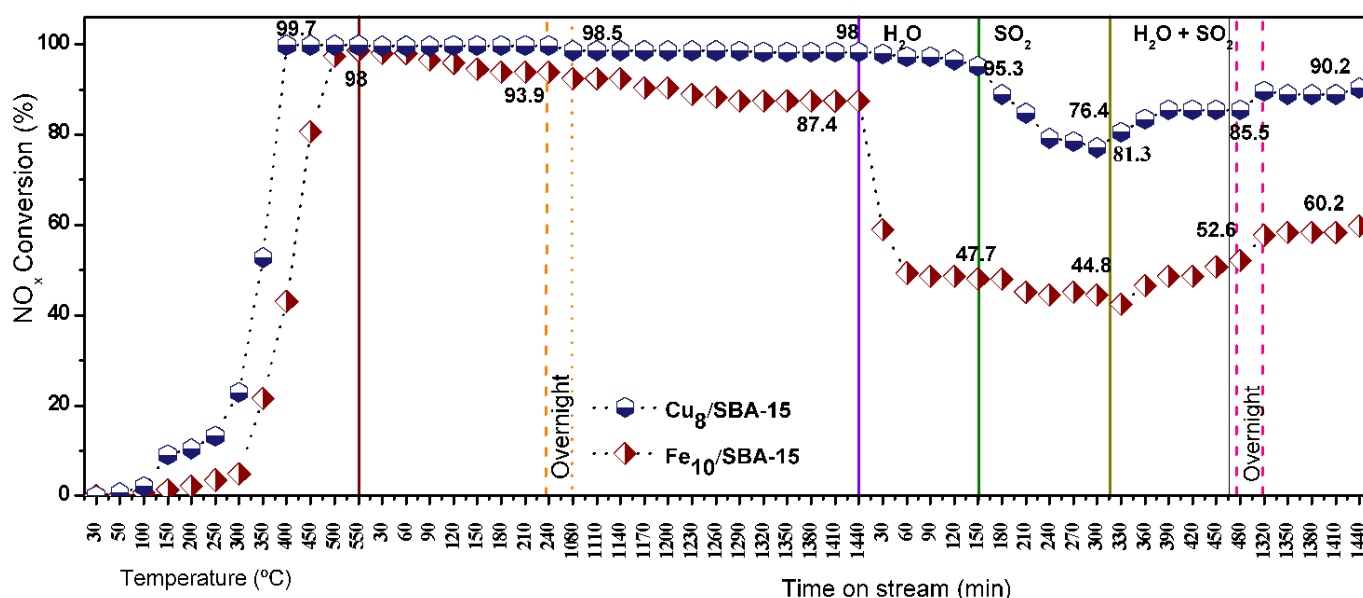


Figure 11. Long term stability runs over $\text{Cu}_8/\text{SBA-15}$ and $\text{Fe}_{10}/\text{SBA-15}$. NO_x conversions obtained in the 30–550 °C temperature range and time on stream intervals of 30–1440 min. The runs were carried out in presence (absence) of steam 10 wt.%, SO_2 50 ppm or both steam 10 wt.% and SO_2 50 ppm.

The activities reach a plateau for $\text{Cu}_8/\text{SBA-15}$ at 400 °C, extending to 500 °C without significant variation in NO_x conversion, while $\text{Fe}_{10}/\text{SBA-15}$ achieves a lower plateau at 500 °C. It must be stressed that the reaction between NO_x and CO occurs favorably around the 300–400 °C temperature window [3], although in most cases, the low temperature region does not favor Fe and Cu sites exhibiting high catalytic ability in this condition.

To distinguish the catalytic effects of different materials, NO_x conversion curves are further obtained at isothermal conditions of 400 and 500 °C to test the durability of solids. An important observation is that the catalytic performances of the solids as a function of time on stream reveals that the NO_x conversions are almost unchanged within 1440 min in the absence of the poisons. Obviously, there are significant dissimilarities in the activity behavior when comparing the performances of $\text{Cu}_8/\text{SBA-15}$ and $\text{Fe}_{10}/\text{SBA-15}$, the latter achieving a NO_x conversion of ca 87.4%. The addition of steam in the reacting gas mixture induced NO_x conversions decay with a $\text{Fe}_{10}/\text{SBA-15}$ activity loss of 40%, while that of $\text{Cu}_8/\text{SBA-15}$ only slightly diminished by 2%. Studies on Fe-based catalysts for the high-temperature water–gas shift reaction illustrate that the reaction between CO and water vapor may take place, forming hydrogen and carbon dioxide under the condition tested [55]. Thus, NO_x reduction by the CO reaction occurrence is impelled when steam is purged in the mixture with the side water–gas shift reaction over the $\text{Fe}_{10}/\text{SBA-15}$ prevalence; consequently, a decrease in the NO_x ability to react with CO on Fe sites in a certain extent decreases the catalytic performance of the solid. The subsequent addition of steam SO_2 to the reaction mixture allows both catalysts to experience an activity decrement with poor poisoning tolerance to SO_2 for $\text{Cu}_8/\text{SBA-15}$ in contrast to NO_x conversion over $\text{Fe}_{10}/\text{SBA-15}$ that drops from 47.7 to 44.8%. As discussed in several studies, the SO_2 presence in the reaction media is inevitably adsorbed on the catalyst surface and competes

with the substrates, which decreases the catalytic activities [56,57]. Furthermore, the NO_x conversion drop is noticeable for both catalysts upon addition of SO₂ steam and water vapor simultaneously in the reaction mixture due to competitive adsorption between SO₂ and the steam on the active sites of the catalysts instead of CO and NO_x, as aforesaid. The NO_x conversions gradually decreased after adding these poisons but their activities are soon restored and this effect is more unfavorable for Fe₁₀/SBA-15 with respect to Cu₈/SBA-15. Moreover, SO₂ may react with H₂O provoking little effect on catalytic performances owing to the reversible sulfation on Cu and Fe sites provided by steam at relatively high temperatures [56]. Suppression of both poisons also allows recovery of the activities of the solids almost to their original levels before the poisoning, resulting in nearly stable NO_x conversion of ca. 90% for Cu₈/SBA-15 while Fe₁₀/SBA-15 is 60% within 1440 min.

Given the good resistance of the solids against the poisoning by steam and SO₂ present in the reaction mixture, the recyclability of the solids at 550 °C is investigated (Figure S3, supplementary materials). A well-known property of Fe and Cu mesoporous materials is their high regenerability towards oxygen. Thus, the catalytic activities of the solids give complete NO_x conversions after the first cycle of use, e.g., 8 h. After the second cycle of use, the Cu₈/SBA-15 catalyst maintains a high activity with a minor performance showed by losses from 98 to 71% for Fe₁₀/SBA-15, after the 4th cycle of use. The lower performance of Fe₁₀/SBA-15 can be read as the promoting effects of CO and NO_x adsorption on the Fe₂O₃ clusters, which weakens one of the Fe-O bonds to create a loosely attached O site. The resultant CO oxidation by the O transformation in the cluster to Fe²⁺ gives the NO reduction via multiple oxidation and NO_x reduction by CO, as found elsewhere [48]. However, the Fe species reduction may be the leading cause of catalyst deactivation. In contrast, the Cu species exist as very small clusters in Fe₁₀/SBA-15 that are well-dispersed on SBA-15, which are responsible for enhanced acidic and redox properties by promoting CO-SCR activity, and to tolerate SO₂ and steam poisoning.

3. Materials and Methods

3.1. Materials

Pluronic 123 (triblock poly(ethylene oxide)-poly(propylene oxide)-poly(ethylene oxide) (PEO-PPO-PEO copolymers, 99.2%) and tetraethyl orthosilicate (TEOS, 99.9%) were purchased from Sigma-Aldrich (Sigma-Aldrich, St. Louis, MO, USA). Iron(III) nitrate nonahydrate (Fe(NO₃)₃ 9H₂O, 99.9%), copper(II) nitrate trihydrate (Cu(NO₃)₂ 3H₂O, 99.9%) and hydrochloric acid (HCl 37.0 wt.%,) were obtained from Vetec (Vetec, Sao Paulo, Brazil). All chemicals were of analytical reagent grade and used without further purification.

3.2. Catalyst Preparation

The support used for the preparation of catalysts was a siliceous SBA-15, which was synthesized following a conventional method [6]. Typically, 0.0004 mols of Pluronic 123 and 4.41 mols of ultrapure water were added to a beaker with 12 mL of HCl under constant stirring at room temperature. Thereafter, about 0.025 mol of the TEOS was added to the previous mixture to aging for 20 h. The mixture was subsequently submitted to hydrothermal treatment in a Teflon-lined autoclave at 100 °C for 48 h. The resulting solid was washed as many times as necessary in order to completely remove the chloride ions and subsequently centrifuged, dried and calcined at 550 °C with a rate of 5 °C min⁻¹ under flowing air.

The prepared Cu_x/SBA-15 and Fe_x/SBA-15 catalysts with x wt.% metal nominal loading were prepared using the wet impregnation method. The 20 mL of hydroalcoholic copper(II) nitrate solution was added to 1 g of the calcined SBA-15 support in a rotatory evaporator system and the mixture was kept at 70 °C for 30 min under vigorous stirring. After preparation, the solid was dried under vacuum for 24 h and then calcined at 550 °C for 6 h. The sample was denoted as Cu_x/SBA-15, with the subscript *x* corresponding to 2, 4, 6 and 8 wt.%. The Fe_x/SBA-15 catalysts were prepared by following the abovementioned

method using iron(III) nitrate as precursor. Similarly, the Fe-containing samples were prepared with iron nominal content close to 2, 4, 6 and 10 wt.%.

3.3. Catalyst Characterizations

X-ray powder diffraction (XRD) was conducted in a Bruker D2 Phaser diffractometer (Bruker, Karlsruhe, Germany) at small and wide angles. The CuK α radiation was used at 30 kV and 10 mA with a step size of 0.01° and 0.3 accumulations per second. Assignment of crystalline phase was through the Joint Committee of Powder Diffraction Standard (JCPDS). The particle size was determined using the Scherer equation from the $2\theta = 35.4^\circ$ (002) plane for CuO phase, whereas the particle size of the Fe₂O₃ is taken from the $2\theta = 35.8^\circ$ (104) plane.

Electron paramagnetic resonance (EPR) measurements for selected samples were carried out in a Bruker spectrometer (Bruker, Rheinstetten, Germany) with a frequency modulation of 100 kHz. All the data were acquired using the X-band microwave frequencies at 9.5 GHz.

Mössbauer spectroscopy measurements were performed in the transmission mode at room temperature in a SEE Co spectrometer (Minneapolis, MN, USA). The gamma photons were provided by a ⁵⁷Co:Rh source with 25 mCi activity. Isomer shifts are reported with respect to α -iron.

Transmission electron microscopy (TEM) micrographs for selected samples were recorded on a Tecnai G2 F20 S-TWIN microscope (FEI, Hillsboro, OR, USA) using an accelerating voltage of 200 kV. Samples were previously dispersed in ethanol and dispersed in the copper grid to perform the analyses.

Scanning electron microscopy (SEM) micrographs were obtained in a Quanta-FEG FEI electron microscope at 2 kV (FEI Quanta, Hillsboro, OR, USA). Elemental analyses were carried out through energy dispersive spectroscopy (EDS) in a scanning electron microscope from Hitachi TM 3000 (Tokyo, Japan), which was equipped with an EDS Swift Ed 3000 system at 15 kV. Before the analyses, the samples were sputtered with gold to improve the conduction.

The micro-Raman scattering spectra measurements were conducted in a triple-grating spectrometer Jobin Yvon from Horiba T64000 model, which was equipped with a N₂-cooled charge-coupled device (CCD) detection system coupled (Horiba, Gloucestershire, UK). The room temperature Raman spectra were collected from 50 to 1000 cm⁻¹. A He–Ne laser wavelength of 532 nm was used with a power of 2 mW for excitation, and a microscope lens with a numerical aperture of 0.35 was used to focus the laser on the sample surface.

X-ray photoelectron spectra (XPS) were recorded with a physical electronics VersaProbe II spectrometer (Minneapolis, MN, USA) using a monochromatic Al K α (1486.6 eV) X-ray source and a charge neutralizer operating at a vacuum better than 10⁻⁷ Pa. Spectra were recorded at 22 °C, using an analyzer pass energy of 29.35 eV, an X-ray power of 47.8 W, and 200 μ m of area analysis. Samples containing Cu were first analyzed with a short irradiation time of 10 min to avoid photo-reduction of Cu. Spectra treatment was performed using the Multipak 9.0 software. Gaussian–Lorentzian curves and nonlinear–Shirley background subtraction were used for peak fitting. During data processing of the XPS spectra, binding energy (BE) values were referenced to the C 1s peak at 284.8 eV of adventitious carbon.

3.4. Catalytic Evaluation in CO-SCR Reaction

The selective catalytic reduction of NO_x by CO (CO-SCR) reaction was carried out in a fixed bed quartz reactor at atmospheric pressure. In each run, 0.150 g of the catalyst were transferred into the reactor and in situ activated in helium at 350 °C for 1 h, prior to testing for their activity in the CO-SCR reaction.

The gaseous mixture consisting of He (99.995%) co-feed to NO_x (7500 ppm) and CO (20,000 ppm) was diluted in helium and introduced to the catalyst bed. The gases were obtained from White Martins. The targeted typical reaction conditions corresponded to

a simulated CO conversion close to 99% [6], where the total flow rate was 80 mL min⁻¹ and the gas hourly space velocity (GHSV) was 48,000 h⁻¹. The reactor temperature was ramped from 50 to 550 °C at 2 °C min⁻¹. Unless noted otherwise, these typical conditions were varied by adding O₂ concentrations of 250, 500 or 1000 ppm. Additionally, experiments were carried out in the absence of oxygen. At a fixed NO_x content of 500 ppm, the NO_x to CO molar ratios of 1:2, 1:1.5 and 1:1 was examined for CO amounts of 1000, 750 and 500 ppm, respectively. The gaseous products were analyzed by a system consisting of a CO/O₂/SO₂/NO/NO_x electrochemical flue gas analyzer from Seitron model chemistry 400.

The poisoning experiments consisted of introducing 500 ppm of NO co-feed by 1000 ppm of CO and balance with He. Either 10 wt.% of steam or 50 ppm of SO₂ (or both) were bubbled through the reactor with the reaction being monitored under the same conditions in the absence of the poisons. Another experiment was carried out feeding a mixture containing 10 wt.% steam, 50 ppm SO₂, 500 ppm NO and 1000 ppm CO in a N₂ stream to the reaction at a steady state to evaluate the resistance against deactivation of the most active solids for 24 h using a velocity of 48,000 h⁻¹.

The NO_x conversion was determined as follows

$$\% X_{\text{NO}_x} = \frac{[\text{NO}_x]_{\text{in}} - [\text{NO}_x]_{\text{out}}}{[\text{NO}_x]_{\text{in}}} \times 100 \quad (1)$$

where X_{NO_x} denotes the NO_x conversion. The terms $[\text{NO}_x]_{\text{in}}$ and $[\text{NO}_x]_{\text{out}}$ represent the steady state concentrations of NO_x in the inlet and outlet, respectively.

The turnover frequency (TOF) catalysts were calculated using first order kinetics for the SCR reaction, according to Equation (2).

$$\text{TOF} = \frac{\text{mol NO}_x \text{ converted}}{\text{mol active metal} \times \text{time}} \quad (2)$$

For recyclability studies, the most active solids were submitted to 500 ppm NO and 1000 ppm CO reaction mixture at GHSV = 48,000 h⁻¹ at 550 °C. After four consecutive cycles of uses, the solids were regenerated using a 1000 ppm of O₂ flushed by He at 550 °C for 2 h.

4. Conclusions

A series of Fe_x/SBA-15 and Cu_x/SBA-15 catalysts was obtained through direct synthesis and post-synthetic incipient wetness impregnation methods with metal loadings of Cu or Fe viz., 2, 4, 6, 8 and 10 wt.%. After the incorporation of metals, the ordered structure of SBA-15 was maintained for metal loadings lower than 4 wt.% with the existence of Cu²⁺ and Fe³⁺ species included into the mesoporous silicate. At higher metal loadings, the formation of α-Fe₂O₃ and CuO phases, in addition to Fe and Cu silica clusters, was found in elevated amounts on solid surface. The impacts of the temperature, NO_x to CO molar ratios, presence of oxygen and poisoning by steam and SO₂, as well as the regenerability on the catalytic activity, demonstrated that surface Fe and Cu were advantageous in the CO-SCR reaction, especially at mild temperatures as low as 350 °C. When steam and SO₂ poisons were used, a significant deactivation of Fe₁₀/SBA-15 was observed. In contrast, active copper species in the silicate form associated with CuO clusters on the surface were more stable against the poisoning effects in Cu₈/SBA-15. The catalytic performance of the Fe₁₀/SBA-15 and Cu₈/SBA-15 catalysts was correlated with the redox properties of the solids, the presence of Cu or Fe supported metals and the formation of highly stable surfaces of Cu clusters that exhibited remarkable regenerability over 48 h.

Supplementary Materials: The following supporting information can be downloaded at: <https://www.mdpi.com/article/10.3390/catal13030527/s1>, Figure S1. XRD patterns of the samples in study; Figure S2. Turnover frequency (TOF) as a function of the temperature for distinct NO_x to

CO molar ratios over Cu₈/SBA-15 and Fe₁₀/SBA-15 samples; Figure S3. Recyclability studies over Fe₁₀/SBA-15.

Author Contributions: M.S.S., J.A.S.R., A.J.M., A.C., R.F.J., G.D.S. and M.A.M.T. performed the experiments; A.C.O. and E.R.-C. analyzed the data and wrote the manuscript, funding acquisition and conceptualization; R.S.A., G.D.S., M.A.M.T. and A.C. designed and performed the experiments and analyzed the data, as well. All authors have read and agreed to the published version of the manuscript.

Funding: The authors acknowledge the financial support by the Funcap (Grant PS1-0186-00346.01.00/21). A.C.O. and ERC thank to Ministerio de Ciencia e Innovación (Spain) projects PID2021-126235OB-C32 and TED2021-130756B-C31, and FEDER funds.

Data Availability Statement: Not applicable.

Acknowledgments: The authors also acknowledge the Central Analítica da Universidade Federal do Ceará for providing the SEM and elemental analysis. Research Fund for J.M. scholarship by CNPq is gratefully acknowledged. M.S. acknowledges the support from the CAPES for her master scholarship.

Conflicts of Interest: The authors declare no conflict of interest.

References

1. Xue, H.; Guo, X.; Mao, D.; Meng, T.; Yu, J.; Ma, Z. Phosphotungstic acid-modified MnO_x for selective catalytic reduction of NO_x with NH₃. *Catalysts* **2022**, *12*, 1248. [[CrossRef](#)]
2. Lin, D.; Zhang, L.; Liu, Z.; Wang, B.; Han, Y. Progress of selective catalytic reduction denitrification catalysts at wide temperature in carbon neutralization. *Front. Chem.* **2022**, *10*, 946133. [[CrossRef](#)]
3. Nascimento, J.P.S.; Oton, L.F.; Oliveira, A.C.; Rodríguez-Aguado, E.; Rodríguez-Castellón, E.; Araujo, R.S.; Souza, S.M.; Lang, R. Selective catalytic reduction of NO_x by CO over doubly promoted MeMo/Nb₂O₅ catalysts (Me = Pt, Ni, or Co). *Catalysts* **2020**, *10*, 1048. [[CrossRef](#)]
4. Mrad, R.; Aissat, A.; Primo, R.; Courcot, D.; Siffert, S. Catalysts for NO_x selective catalytic reduction by hydrocarbons (HC-SCR). *Appl. Catal.* **2015**, *504*, 542–548. [[CrossRef](#)]
5. Zhang, Y.; Zhao, L.; Kang, M.; Chen, Z.; Gao, S.; Hao, H. Insights into high CO-SCR performance of CuCoAlO catalysts derived from LDH/MOFs composites and study of H₂O/SO₂ and alkali metal resistance. *Chem. Eng. J.* **2021**, *426*, 131873. [[CrossRef](#)]
6. Souza, M.S.; Araújo, R.S.; Oliveira, A.C. Optimizing reaction conditions and experimental studies of selective catalytic reduction of NO by CO over supported SBA-15 catalyst. *Environm. Sci. Pollution Res.* **2020**, *27*, 30649–30660. [[CrossRef](#)] [[PubMed](#)]
7. Zang, P.; Liu, J.; Zhang, G.; Jia, B.; He, Y.; Wang, Y.; Lv, Y. Insights into the highly activity CuMgFe oxides for the selective catalytic reduction of NO by CO: Structure-activity relationships and K/SO₂ poisoning mechanism. *Fuel* **2023**, *331*, 125800. [[CrossRef](#)]
8. Nascimento, J.P.S.; Oliveira, A.C.; Araujo, J.C.S.; Sousa, F.F.; Saraiva, G.D.; Rodríguez-Aguado, E.; Rodríguez-Castellón, E. Combined promoting effect of molybdenum on the bimetallic Al₂O₃-La₂O₃ catalysts for NO_x reduction by CO. *Fuel* **2020**, *275*, 117872. [[CrossRef](#)]
9. Boutros, M.; Trichard, J.; Costa, P. Silver supported mesoporous SBA-15 as potential catalysts for SCR NO_x by ethanol. *Appl. Catal.* **2009**, *91*, 640–648. [[CrossRef](#)]
10. Damma, D.; Ettireddy, P.R.; Reddy, B.M.; Smirniotis, P.G. A review of low temperature NH₃-SCR for removal of NO_x. *Catalysts* **2019**, *9*, 349. [[CrossRef](#)]
11. Selleria, T.; Nova, I.; Tronconia, E.; Schmeisser, V.; Seher, S. The impact of light and heavy hydrocarbons on the NH₃-SCR activity of commercial Cu- and Fe-zeolite catalysts. *Catal. Today* **2019**, *320*, 100–111. [[CrossRef](#)]
12. Zhang, R.; Shi, D.; Zhao, Y.; Chen, B.; Xue, J.; Liang, X.; Lei, Z. The reaction of NO + C₃H₆ + O₂ over the mesoporous SBA-15 supported transition metal catalysts. *Catal. Today* **2011**, *175*, 26–33. [[CrossRef](#)]
13. Patel, A.; Thomas, R.E.; Rudolph, V.; Zhu, Z. Selective catalytic reduction of NO by CO over CuO supported on SBA-15: Effect of CuO loading on the activity of catalysts. *Catal. Today* **2011**, *166*, 188–193. [[CrossRef](#)]
14. Guo, K.; Jiaweia, J.; Osuga, R.; Zhu, Y.; Sun, J.; Tang, C.; Kondo, J.N.; Dong, L. Construction of Fe₂O₃ loaded and mesopore confined thin-layer titania catalyst for efficient NH₃-SCR of NO_x with enhanced H₂O/SO₂ tolerance. *Appl. Catal.* **2021**, *287*, 119982. [[CrossRef](#)]
15. Tsoncheva, T.; Gallo, A.; Genova, I.; Spassova, I.; Marelli, M.; Dimitrov, M.; Khristova, M.; Atanasova, G.; Kovacheva, D.; Nihtyanova, D.; et al. Control of copper particles deposition in mesoporous SBA-15 silica by modified CVD method. *Inorganica Chim. Acta.* **2014**, *423*, 145–151. [[CrossRef](#)]
16. Jankowska, A.; Kowalczyk, A.; Rutkowska, M.; Michalik, M.; Chmielarz, L. Catalytic performance of bimetallic systems (Cu-Fe, Cu-Mn, Fe-Mn) based on spherical MCM-41 modified by template ion-exchange in NH₃-SCR process. *Catalysts* **2022**, *12*, 885. [[CrossRef](#)]

17. Rivera-Jiménez, S.M.; Méndez-González, S.; Hernández-Maldonado, A. Metal ($M = \text{Co}^{2+}$, Ni^{2+} , and Cu^{2+}) grafted mesoporous SBA-15: Effect of transition metal incorporation and pH conditions on the adsorption of Naproxen from water. *Microp. Mesop. Mater.* **2010**, *132*, 470–479. [[CrossRef](#)]
18. Miao, K.; Luo, X.; Wang, W.; Guo, J.; Guo, S.; Cao, F.; Hu, Y.; Chang, P.; Feng, G. One-step synthesis of Cu-SBA-15 under neutral condition and its oxidation catalytic performance. *Microp. Mesop. Mater.* **2019**, *289*, 109640. [[CrossRef](#)]
19. Shen, W.; Mao, D.; Luo, Z.; Yu, J. CO oxidation on mesoporous SBA-15 supported CuO-CeO₂ catalyst prepared by a surfactant-assisted impregnation method. *RSC Adv.* **2017**, *7*, 27689–27698. [[CrossRef](#)]
20. Gu, Z.; Cheng, L.; Tan, C.; Sin, S.; Huang, C.; Tang, C. Enriching SO₄²⁻ Immobilization on $\alpha\text{-Fe}_2\text{O}_3$ via Spatial Confinement for Robust NH₃-SCR Denitration. *Catalysts* **2022**, *12*, 991. [[CrossRef](#)]
21. Kumar, M.S.; Pérez-Ramírez, J.; Debbagh, M.N.; Smarsly, B.; Bentrup, U.; Brückner, A. Evidence of the vital role of the pore network on various catalytic conversions of N₂O over Fe-silicalite and Fe-SBA-15 with the same iron constitution. *Appl. Catal.* **2006**, *62*, 244–254. [[CrossRef](#)]
22. Kuśtrowski, P.; Chmielarz, L.; Surman, J.; Bidzińska, E.; Dziembaj, R.; Cool, P.; Vansant, E.F. Catalytic activity of MCM-48-, SBA-15-, MCF-, and MSU-type mesoporous silicas modified with Fe³⁺ species in the oxidative dehydrogenation of ethylbenzene in the presence of N₂O. *J. Phys. Chem.* **2005**, *109*, 9808–9815. [[CrossRef](#)]
23. Volanti, D.P.; Keyson, D.; Cavalcante, L.S.; Simões, A.Z.; Joya, M.R.; Longo, E.; Varela, P.S.; Pizani, P.S.; Souza, A.G. Synthesis and characterization of CuO flower-nanostructure processing by a domestic hydrothermal microwave. *J. Alloys Compd.* **2008**, *459*, 537–542. [[CrossRef](#)]
24. Carmo, J.V.C.; Bezerra, R.C.F.; Tehuacanero-Cuapa, S.; Rodríguez-Aguado, E.; Lang, R.; Campos, A.F.; Duarte, G.; Saraiva, G.D.; Otubo, L.; Oliveira, A.C.; et al. Synthesis of tailored alumina supported Cu-based solids obtained from nanocomposites: Catalytic application for valuable aldehyde and ketones production. *Mater. Chem. Phys.* **2022**, *292*, 126800. [[CrossRef](#)]
25. Tsoncheva, T.; Issaa, G.; Blasco, T.; Dimitrov, M.; Popova, M.; Hernández, S.; Kovacheva, D.; Atanasova, G.; Nieto, J.M.L. Catalytic VOCs elimination over copper and cerium oxide modified mesoporous SBA-15 silica. *Appl. Catal.* **2013**, *453*, 1–12. [[CrossRef](#)]
26. Dantas, N.O.; Ayta, W.E.F.; Silva, A.; Cano, N.F.; Silva, S.W.; Morais, P.C. Effect of Fe₂O₃ concentration on the structure of the SiO₂-Na₂O-Al₂O₃-B₂O₃ glass system. *Spectrochim. Acta A Mol. Biomol. Spectrosc.* **2011**, *81*, 140–143. [[CrossRef](#)]
27. López-Sánchez, J.; Serrano, A.; Campo, A.; Abuín, M.; Fuente, O.R.; Carmona, N. Sol-gel synthesis and micro-Raman characterization of $\epsilon\text{-Fe}_2\text{O}_3$ Micro- and nanoparticles. *Chem. Mater.* **2016**, *28*, 511–518. [[CrossRef](#)]
28. Cruz, M.G.A.; Fernandes, F.A.N.; Oliveira, A.C.; Filho, J.M.; Oliveira, A.C.; Campos, A.F.; Padron-Hernandez, E.; Rodríguez-Castellón, E. Effect of the calcination temperatures of the Fe-based catalysts supported on polystyrene mesoporous carbon for FTS synthesis. *Catal. Today* **2017**, *282*, 174–184. [[CrossRef](#)]
29. Jubb, A.M.; Allen, H.C. Vibrational spectroscopic characterization of hematite, maghemite, and magnetite thin films produced by vapor deposition. *ACS Appl. Mater. Interfaces.* **2010**, *2*, 2804–2812. [[CrossRef](#)]
30. Li, Y.; An, D.; Zhang, Q.; Wang, Y. Copper-catalyzed selective oxidation of methane by oxygen: Studies on catalytic behavior and functioning mechanism of CuO_x/SBA-15. *J. Phys. Chem. C* **2008**, *112*, 13700–13708. [[CrossRef](#)]
31. Popova, M.; Szegedi, A.; Cherkezov-Zheleva, Z.; Dimitrova, A.; Mitov, I. Toluene oxidation on chromium- and copper-modified SiO₂ and SBA-15. *Appl. Catal.* **2010**, *381*, 26–35. [[CrossRef](#)]
32. Guang-Shea, L.; Li-Pinga, L.; Smith, R.L.; Inomata, H. Characterization of the dispersion process for NiFe₂O₄ nanocrystals in a silica matrix with infrared spectroscopy and electron paramagnetic resonance. *J. Mol. Struct.* **2001**, *560*, 87–93. [[CrossRef](#)]
33. Jahagirdar, A.A.; Dhananjaya, N.; Monika, D.L.; Kesavulu, C.R.; Nagabhushana, H.; Sharma, S.C.; Nagabhushana, B.M.; Shivakumara, C.; Rao, J.L.; Chakradhar, R.P.S. Structural, EPR, optical and magnetic properties of $\alpha\text{-Fe}_2\text{O}_3$ nanoparticles. *Acta A Mol. Biomol. Spectrosc.* **2013**, *104*, 512–518. [[CrossRef](#)] [[PubMed](#)]
34. Zhang, L.; Zhao, Y.; Dai, H.; He, H.; Au, C.T. A comparative investigation on the properties of Cr-SBA-15 and CrO_x/SBA-15. *Catal. Today* **2008**, *131*, 42–54. [[CrossRef](#)]
35. Karthikeyan, S.; Pachamuthu, M.P.; Isaacs, M.A.; Kumar, S.; Lee, A.F.; Sekaran, G. Cu and Fe oxides dispersed on SBA-15: A Fenton type bimetallic catalyst for N,N-diethyl-p-phenylenediamine degradation. *Appl. Catal.* **2016**, *199*, 323–330. [[CrossRef](#)]
36. Gütllich, P.; Bill, E.; Trautwein, A.X. *Mössbauer Spectroscopy and Transition Metal Chemistry*; Springer: Berlin/Heidelberg, Germany, 2011.
37. Ge, X.; Li, M.; Shen, J. The Reduction of Mg-Fe-O and Mg-Fe-Al-O Complex Oxides Studied by Temperature-Programmed Reduction Combined with in Situ Mossbauer Spectroscopy. *J. Solid State Chem.* **2001**, *161*, 38–44. [[CrossRef](#)]
38. Bødker, F.; Hansen, M.F.; Koch, C.B.; Lefmann, K.; Mørup, S. Magnetic properties of hematite nanoparticles. *Phys. Rev. B.* **2000**, *61*, 6826–6838. [[CrossRef](#)]
39. Ji, M.; Chen, G.; Wang, J.; Wang, X.; Zhang, T. Dehydrogenation of ethylbenzene to styrene with CO₂ over iron oxide-based catalysts. *Catal. Today.* **2010**, *158*, 464–469. [[CrossRef](#)]
40. Cullity, B.D.; Graham, C.D. *Introduction to Magnetic Materials*, 2nd ed.; IEEE Press and John Wiley & Sons, Inc.: Hoboken, NJ, USA, 2009.
41. Bachari, K.; Millet, J.M.M.; Bonville, P.; Cherifi, O.; Figueras, F. Spectroscopic characterization of iron nanoparticles in Fe-mesoporous silicate catalysts. *J. Catal.* **2007**, *249*, 52–58. [[CrossRef](#)]

42. Neto, A.B.S.; Oliveira, A.C.; Rodriguez-Castellón, E.; Campos, A.F.; Freire, P.T.C.; Sousa, F.F.S.; Filho, J.M.; Araujo, J.C.S.; Rossano Lang, R. A comparative study on porous solid acid oxides as catalysts in the esterification of glycerol with acetic acid. *Catal. Today* **2020**, *349*, 57–67. [[CrossRef](#)]
43. Gamarra, D.; Munuera, G.; Hungria, A.B.; Fernández-García, M.; Conesa, J.C.; Midgley, P.A.; Wang, X.Q.; Hanson, J.C.; Rodríguez, J.A.; Martínez-Arias, A. Structure-activity relationship in nanostructured copper ceria based preferential CO oxidation. *J. Phys. Chem. C* **2007**, *111*, 11026. [[CrossRef](#)]
44. Moulder, J.F.; Stickle, W.F.; Sobel, P.E.; Bomben, K.D. *Handbook of X-ray Photoelectron Spectroscopy*; Chastain, J., Ed.; Perkin-Elmer: Eden Prairie, MN, USA, 1992.
45. Ou, X.; Chen, K.; Wei, L.; Deng, Y.; Li, J.; Li, B.; Dong, L. Effect of Co doping on magnetic and CO-SCR properties of γ -Fe₂O₃. *Ind. Eng. Chem. Res.* **2021**, *60*, 5744–5757. [[CrossRef](#)]
46. Wang, D.; Huang, B.; Shi, Z.; Long, H.; Li, L.; Yang, Z.; Dai, M. Influence of cerium doping on Cu–Ni/activated carbon low-temperature CO-SCR denitration catalysts. *RSC Adv.* **2021**, *11*, 18458–18467. [[CrossRef](#)] [[PubMed](#)]
47. Patel, A.; Shukla, P.; Rufford, T.; Wang, S.; Chen, J.; Rudolph, V.; Zhu, Z. Catalytic reduction of NO by CO over copper-oxide supported mesoporous silica. *Appl. Catal. A. Gen.* **2011**, *409–410*, 55–65. [[CrossRef](#)]
48. Chen, X.; Liu, Y.; Lian, D.; Chen, M.; Ji, Y.; Xing, L.; Wu, K.; Liu, S. Recent advances of Cu-based catalysts for NO reduction by CO under O₂-containing conditions. *Catalysts* **2022**, *12*, 1402. [[CrossRef](#)]
49. Oton, L.F.; Oliveira, A.C.; Araujo, J.C.; Araujo, R.S.; De Sousa, F.F.; Saraiva, G.D.; Lang, R.; Otubo, L.; Duarte, G.C.D.S.; Campos, A. Selective catalytic reduction of NO_x by CO (CO-SCR) over metal-supported nanoparticles dispersed on porous alumina. *Adv. Powder Technol.* **2020**, *31*, 464–476. [[CrossRef](#)]
50. Bai, Y.; Bian, X.; Wu, W. Catalytic properties of CuO/CeO₂-Al₂O₃ catalysts for low concentration NO reduction with CO. *Appl. Surf. Sci.* **2019**, *463*, 435–444. [[CrossRef](#)]
51. Nova, I.; Lietti, L.; Forzatti, P.; Frola, F.; Prinetto, F.; Giovanna Ghiott, G. Reaction pathways in the reduction of NO_x species by CO over Pt–Ba/Al₂O₃: Lean NO_x trap catalytic systems. *Top Catal.* **2009**, *52*, 1757–1761. [[CrossRef](#)]
52. Ye, D.; Ren, X.; Qu, R.; Liu, S.; Zheng, C.; Gao, X. Designing SO₂-resistant cerium-based catalyst by modifying with Fe₂O₃ for the selective catalytic reduction of NO with NH₃. *Mol. Catal.* **2019**, *462*, 10–18. [[CrossRef](#)]
53. Palomares, A.E.; López-Nieto, J.M.; Lázaro, F.J.; López, A.; Corma, A. Reactivity in the removal of SO₂ and NO_x on Co/Mg/Al mixed oxides derived from hydrotalcites. *Appl. Catal.* **1999**, *20*, 257–266. [[CrossRef](#)]
54. Fan, B.; Zhang, Z.; Liu, C.; Liu, Q. Investigation of sulfated iron-based catalysts with different sulfate position for selective catalytic reduction of NO_x with NH₃. *Catalysts* **2020**, *10*, 1035. [[CrossRef](#)]
55. Zhu, M.; Wachs, I.E. Iron-based catalysts for the high-temperature water–gas shift (HT-WGS) reaction: A Review. *ACS Catal.* **2016**, *6*, 722–732. [[CrossRef](#)]
56. Gao, C.; Shi, J.-W.; Fan, Z.; Gao, G.; Niu, C. Sulfur and water resistance of Mn-based catalysts for low-temperature selective catalytic reduction of NO_x: A Review. *Catalysts* **2018**, *8*, 11. [[CrossRef](#)]
57. Ilieva, L.; Pantaleo, G.; Velinov, N.; Tabakova, T.; Petrova, P.; Ivanov, I.; Avdeev, G.; Paneva, D.; Venezia, A.M. NO reduction by CO over gold catalysts supported on Fe-loaded ceria. *Appl. Catal.* **2015**, *174–175*, 176–184. [[CrossRef](#)]

Disclaimer/Publisher’s Note: The statements, opinions and data contained in all publications are solely those of the individual author(s) and contributor(s) and not of MDPI and/or the editor(s). MDPI and/or the editor(s) disclaim responsibility for any injury to people or property resulting from any ideas, methods, instructions or products referred to in the content.